International Journal of Rock Mechanics & Mining Sciences 147 (2021) 104916

Contents lists available at ScienceDirect

International Journal of Rock Mechanics and Mining Sciences

journal homepage: www.elsevier.com/locate/ijrmms

Effect of water on sandstone's fracture toughness and frictional parameters: Brittle strength constraints

Corentin Noël [a,*], Patrick Baud [b], Marie Violay [a]

[a] Laboratory of Experimental Rock Mechanics, École Polytechnique Fédérale de Lausanne, Lausanne, Switzerland
[b] Université de Strasbourg, CNRS, Institut Terre et Environnement de Strasbourg, UMR 7063, 5 Rue René Descartes, Strasbourg F, 67084, France

ARTICLE INFO

Keywords:
Water weakening
Fracture toughness
Friction
Compressive strength
Sandstones
Micro-mechanical model

ABSTRACT

Water presence causes a dramatic reduction of sandstone strength. Under compressive stress conditions, the strength of a rock sample is controlled by frictional parameters and the fracture toughness of the material. Here, we report fracture toughness, frictional and uniaxial compression tests performed on five sandstones under dry and water-saturated conditions, that provide new insight into the mechanical influence of water on sandstone strength. The mechanical data show that water saturation causes a reduction of i) the fracture toughness and fracture energy ranging from 6 to 35% and 21–52%, respectively; and ii) the static friction coefficient ranging from 0 to 19%. The results suggest that the water weakening in sandstones (with a reduction of the uniaxial compression strength ranging from 0 to 30%) is due to the reduction of the fracture toughness and of the static friction coefficient of the materials. The measured fracture toughness and frictional parameters are then introduced into two micro-mechanical models (a pore-emanating cracks model and a wing crack model) to predict the water weakening. It is shown that the models predict the water weakening relatively well with a general slight overestimation (10–20%). Finally, a parametric analysis on the wing crack model revealed that a sandstone's absolute strength can be estimated by means of combined physical and mechanical parameter measurements.

1. Introduction

Among the environmental parameters affecting rock mechanical behaviour and strength, the presence of fluid, particularly water, has been shown to be primordial. Because it is meaningful for many applications including earthquake nucleation, landslide triggering, reservoir stimulation, mining, geotechnics, etc., rock-fluid interactions have been widely studied. Water weakening has been reported in most types of rocks such as sandstones,[1–3] carbonates,[4,5] tuff[6] or basalts.[7] The primary mechanical effect of fluid is to reduce the effective stress acting on the rock mass.[8] Under isotropic mechanical behaviour, the effective stresses are defined by $\sigma^{eff} = \sigma - AP_f$, where σ is the macroscopic stress P_f if the pore fluid pressure and A is the effective stress coefficient, which depends on the rock and measured properties. Following the work of Terzaghi for soils, it has been shown that for rock strength and under drained pore fluid conditions, A is close to (or equal to) unity.[9–11] For porous sandstones, the effective pressure coefficient for brittle strength and shear-enhanced compaction were also observed to be very close to unity.[12] Additionally, water favours rock-fluid interactions, weakening the rock mass by activating mechanisms such as: stress corrosion cracking[13–17] or mineral dissolution/alteration.[18]

Among the studies on rock water weakening, the largest published sets of experimental data are on sandstones. These data sets have shown that water-saturated sandstones can present a lower uniaxial and triaxial strength than dry samples. For example, Berea, Darley Dale, Flechtingen, Pennant sandstones or different Buntsandstein unit sandstones from Soultz-sous-Forêts (France) present a water weakening of 8, 14, 40, 43 and 20–40%, respectively.[1,19–21] However, other sandstones like Fontainebleau show no strength weakening in the presence of water.[2,22] Hawkins & McConnell[3] studied the effect of moisture content on 35 British sandstones, and found that the strength sensitivity to water is dependent on the quartz and clay mineral content: the higher the quartz and the lower the clay contents, the less sensitive the sandstone strength is to water saturation.

Under compressive stress, rock failure originates from the nucleation, propagation and coalescence of micro-cracks. In turn, micro-crack growth is primarily controlled by 1) the frictional parameters of the pre-existing cracks, and 2) the fracture toughness of the non-damaged material.[23–25] Based on classical micro-mechanical models, Baud et al.[1] indeed interpreted water weakening in four sandstones, both in

* Corresponding author.
E-mail address: corentin.noel@uniroma1.it (C. Noël).

https://doi.org/10.1016/j.ijrmms.2021.104916
Received 1 April 2021; Received in revised form 21 July 2021; Accepted 10 September 2021
Available online 16 September 2021

the brittle and cataclastic flow regimes, due to a reduction of both of these parameters in the presence of water. However, the respective contribution of these parameters to the water weakening of rocks is poorly constrained by systematic measurements.

Experimental studies on the effect of water on frictional parameters of rock surfaces have shown that static friction coefficient (i.e., the shear stress normalised by the normal stress acting on a rock surface (e.g., joint, discontinuity, fault …) at the onset of sliding) is reduced in the presence of water for granite,[26] quartzite,[27] limestone,[28] and granitic gneiss.[29] For example, Jaeger[29] and Zhang[30] found a reduction of the static friction coefficient ranging from 2 to 10% in the presence of water compared to dry conditions for different sandstones. Two main possibilities can explain such a reduction: 1) water decreases the adhesion forces at contact points, and 2) water reduces the strength of the asperities supporting the shear stress. Additionally, a reduction of the fracture toughness of rocks in the presence of water has been interpreted as due to: stress corrosion,[31] mineral dissolution,[32] capillary forces at the crack tip,[33] clay weakening,[34] grain contact lubrication,[35] or a reduction of surface energy via adsorption mechanisms.[1] For instance, for sandstones, the presence of water causes a reduction of the mode I fracture toughness typically ranging from 30 to 50% compared to dry conditions.[32,33,35]

In summary, under drained conditions and at an equivalent effective stress, the presence of water can reduce the macroscopic rock strength via the reduction of fracture toughness and the static friction coefficient. The weakening mechanisms are mechanical and chemical processes that occur at the microscopic (i.e., grain) scale. A plethora of mechanisms can explain such water weakening, and depend on a defined set of conditions (i.e., pressure, temperature, strain rate, etc.) and/or rock type. However, for simple experimental conditions and a defined rock type, it is not clear if one (or more) mechanisms prevail over the others.

Here, we address the following questions: 1) do systematic measurements of the fracture toughness and static friction coefficient reveal a significant reduction under water-saturated conditions compare to dry conditions? 2) Since water weakening in sandstones may depend on the quartz and clay mineral content, are the measured fracture toughnesses and static friction coefficient coefficients in direct agreement with this? 3) How do new data improve the micro-mechanical interpretation of water weakening in sandstones? To answer these questions, we measured the effect of water on the uniaxial compressive strength (UCS) of five sandstones to quantify their water weakening. Then, the mode I fracture toughness and static friction coefficient were measured under dry and water-saturated conditions in order to constrain the relative influence of the involved parameters. These measured mechanical parameters are used in micro-mechanical models aiming to better constrain the physico-chemical mechanisms involved in the water weakening of sandstones.

2. Experimental methodology

2.1. Starting materials

Five sandstones were used in this study: Fontainebleau sandstone (FS) (south of Paris, France), Bentheim sandstone (BS) (Bentheim, Germany), Adamswiller sandstone (AS) (Bas-Rhin, France), Rothbach sandstone (RS) (Bas-Rhin, France), Darley Dale sandstone (DS) (Derbyshire, England). These sandstones were chosen because they span a wide range of initial porosities and different mineral compositions (Table 1), and because their mechanical properties are well documented in the literature.[2,22,36–43]

In order to characterize the tested sandstones, X-ray crystallography and optical microscopic surveys were first performed (Table 1 and Fig. 1). These surveys revealed that FS and BS are almost pure quartz sandstones (97 and 89%, respectively). In addition to quartz grains, AS and RS are also composed of a high quantity of K-feldspar (73 and 57% of quartz, and 17 and 35% of K-feldspar, respectively). DS is mainly composed of quartz (69%), plagioclase (10%) and K-feldspar (10%). The tested sandstones have a phyllosilicate (i.e., including mica and clay mineral) content ranging from 3 to 9%. The optical microscopic survey revealed that the average grain sizes of FS, BS, AS, RS and DS are 200, 200, 135, 250 and 220 μm, respectively. The porosity of the five sandstones can be divided into equant pores (i.e., more or less spherical pores) and grain contacts that form elongated cracks (Fig. 1). FS, BS, AS, RS and DS have equant pores of diameter ranging from 10 to 100, 20 to 100, 6 to 60, 15 to 200 and 20–100 μm, respectively; their cracks linearly extend from 200 to 400, 200 to 600, 135 to 400, 250 to 900 and 220–650 μm, respectively.

Then, prior deformation, porosity and ultrasonic *P*- and *S*-wave propagation velocities were measured at room pressure and temperature to ensure experiment reproducibility. From these measurements, the dynamic elastic moduli were inferred.

Porosities and bulk densities of the sandstones were measured using the triple weight method (i.e., weighing the sample dry, saturated, and saturated and immersed) assuming Archimedes' principle0.[44] The five tested sandstones have initial porosities ranging from 5 to 25% and bulk densities ranging from 2000 to 2500 g/cm^3 (Table 1).

Ultrasonic *P*- and *S*-wave velocities were measured at room pressure and temperature using two *P*- and *S*-wave piezoelectric transducers (*Olympus V103-RB* and *Olympus V153-RB*, respectively). The electrical signal was delivered by a generator at 1-MHz frequency and recorded with a numerical oscilloscope. The time of the *P*- and *S*-wave arrivals were handpicked and used to compute the *P*- and *S*-wave velocities across the samples (V_p and V_s, respectively). The measurements were performed both under dry and water-saturated conditions. The obtained values for V_p and V_s are directly linked to the sample porosity, with decreasing velocity values for higher sample porosities (Table 1).

Assuming that the samples are isotropic (note that BS, AS and RS present a slight transverse anisotropy), their dynamic elastic moduli

Table 1
Mineral composition and physical properties of the five studied sandstones. Abbreviations: qtz = quartz, mic = mica, phl = phyllosilicates, chl = chlorite, kao = kaolinite, kfs = K-feldspar, ab = Na-plagioclase, dol = dolomite, ill = illite, smc = smectite, hm = hematite.

Sample	Mineral composition	Average grain size (μm)	Porosity (%)	Bulk dry density (g/cm^3)	Vp (m/s)		Vs (m/s)	
					dry	saturated	dry	saturated
Fontainebleau	97% qtz, 3% mic	200	4.99 ± 0.7	2526 ± 52	3643 ± 566	4562 ± 324	2210 ± 431	2631 ± 198
Bentheim	89% qtz, 8% phl (1% chl, 7% kao), 2% kfs, 0.6% ab, 0.8% dol	200	24.0 ± 0.2	2010 ± 9	2965 ± 76	3198 ± 206	1850 ± 48	1840 ± 94
Adamswiller	73% qtz, 9% phl (4% mic, 0.2% ill/smc, 3% chl, 2% kao), 17% kfs, 0.7% hm	135	24.3 ± 0.4	2011 ± 16	2516 ± 113	2921 ± 122	1621 ± 40	1513 ± 63
Rothbach	57% qtz, 6% phl (5% mic, 1% ill/smc, 0.3% chl, 0.3% kao), 35% kfs	240	19.9 ± 0.4	2117 ± 15	3022 ± 113	3413 ± 201	2002 ± 48	1955 ± 79
Darley Dale	69% qtz, 9% phl (0.2% mic, 0.6% chl, 8% kao), 10% kfs, 10% ab	220	15.3 ± 0.6	2243 ± 21	2985 ± 58	3454 ± 176	1994 ± 60	1924 ± 111

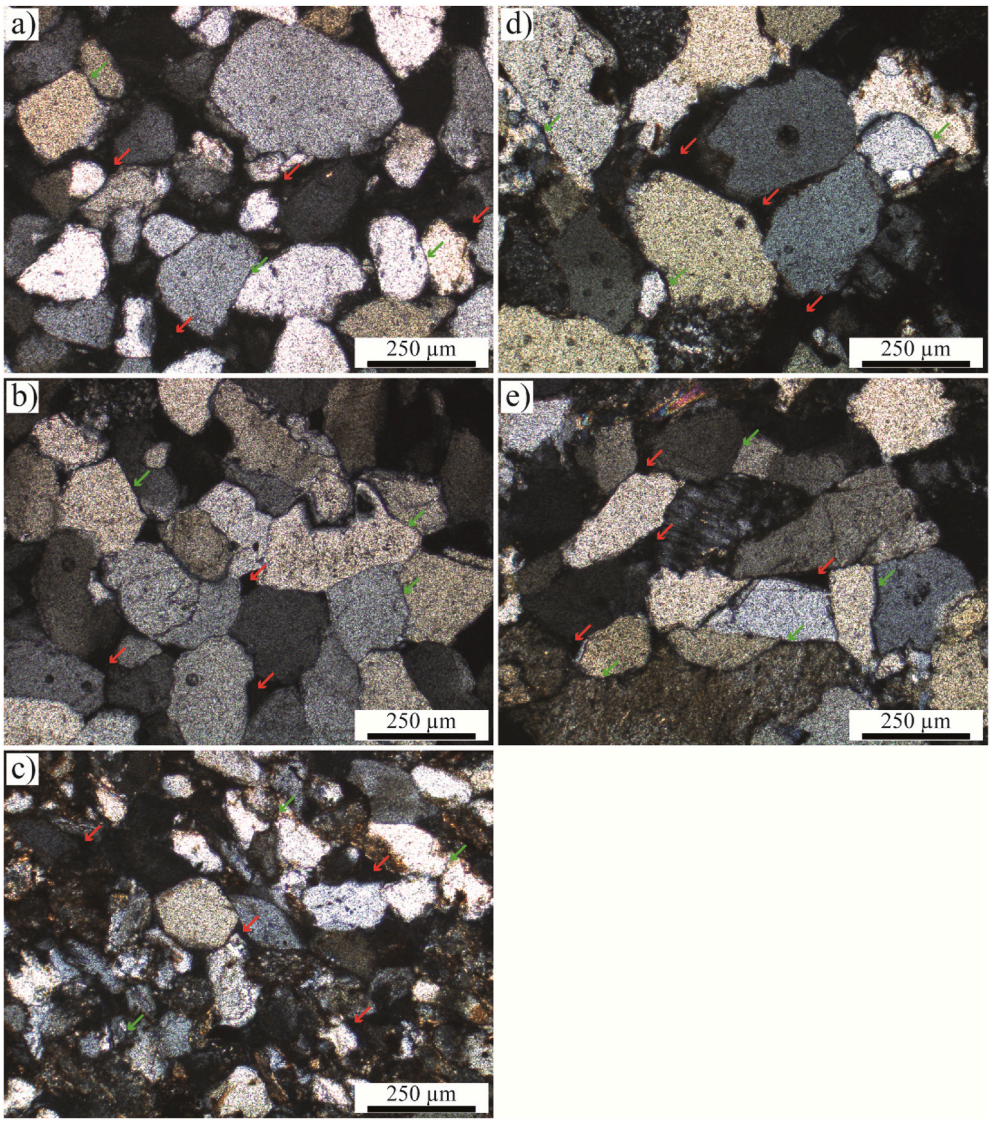

Fig. 1. Optical micrographs under a cross-polarized microscope of a) Fontainebleau sandstone, b) Bentheim sandstone, c) Adamswiller sandstone, d) Rothbach sandstone and e) Darley Dale sandstone. The red and green arrows show equant pores and cracks at the grain junctions, respectively. (For interpretation of the references to colour in this figure legend, the reader is referred to the Web version of this article.)

have been computed from the measured porosity (ϕ), density (ρ), V_p and V_s, following the ASTM Standard[45]:

$$E = \frac{\left[\rho V_s^2\left(3V_p^2 - 4V_s^2\right)\right]}{\left(V_p^2 - V_s^2\right)} \quad (1)$$

$$G = \rho V_s^2 \quad (2)$$

$$K = \lambda + \frac{2G}{3} \quad (3)$$

$$\lambda = \rho V_p^2 - 2G \quad (4)$$

$$\nu = \frac{\left(V_p^2 - 2V_s^2\right)}{2\left(V_p^2 - V_s^2\right)} \quad (5)$$

where E, G, K, λ, and ν are the Young, shear, and bulk moduli, Lamé's first parameter and Poisson's ratio, respectively (Table 2).

Table 2
Dynamic elastic parameters obtained from the dry *P*- and *S*-wave velocity survey (i.e., equations (1)–(5)) for the five tested sandstones.

Sample	Dynamic Young's modulus, E (GPa)	Dynamic shear modulus, G (GPa)	Dynamic bulk modulus, K (GPa)	Dynamic Lamé's 1st parameter, λ (GPa)	Dynamic Poisson's ratio, ν
Fontainebleau	30.3 ± 10.7	12.7 ± 4.9	17.2 ± 4.8	34.2 ± 10.5	0,20 ± 0.07
Bentheim	16.2 ± 0.8	6.9 ± 0.4	8.5 ± 0.7	17.7 ± 0.9	0,18 ± 0.02
Adamswiller	12.1 ± 0.7	5.3 ± 0.3	5.7 ± 0.7	12.7 ± 0.9	0,14 ± 0.03
Rothbach	18.8 ± 1.2	8.5 ± 0.4	8.0 ± 1.2	19.4 ± 1.5	0,11 ± 0.04
Darley Dale	19.4 ± 0.5	8.9 ± 0.6	8.1 ± 1.3	20.0 ± 0.7	0,09 ± 0.06

2.2. Experimental methods

Three different types of experiments were performed in this study: uniaxial compression, fracture toughness and friction experiments. They required different specific initial sample geometries, deformation apparatuses, experimental procedures and data analyses. The following is divided into three methodology sections, one for each type of experiment.

In order to understand how water influences the mechanical behaviour of sandstones, the experiments were performed under both dry and water-saturated conditions. In the following, "dry experiment" refers to experiments performed with samples that have been placed in an oven for at least 12 h and then placed in a desiccator at room temperature for at least 5 h prior to deformation at room temperature. For all setups (uniaxial compression, fracture toughness and friction experiments), "saturated experiment" refers to experiments performed with samples that have been first placed in an oven for at least 12 h, then saturated under vacuum with de-aired distilled water at ambient pressure and temperature. Additionally, the saturated experiments were all performed under immersed (i.e., samples immersed into distilled water during their deformation) and drained conditions. Note that, even if in sandstones the porosity is highly connected,[42] potential isolated pores cannot be saturated. Note also that the characteristic time for water to diffuse across the entire sample is less than 1 s for all the sandstones used (see Noël et al.[46]).

In the following sample preparation processes, tap water was used as cooling fluid and that samples were prepared from unique blocks to reduce inhomogeneity.

2.2.1. Uniaxial compression

For the uniaxial compression experiments, samples were first diamond drilled to a diameter of 36- or 28-mm, depending on available materials. Cylinders were then sawed and the opposite faces ground flat in order to prevent any parallelism defects (±50-μm precision) for a final length of 72 or 56 mm (i.e., twice the sample diameter). For BS, AS and RS, bedding planes were clearly visible, and samples were cored with the planes perpendicular to the sample axis (Fig. 2a).

The uniaxial compression experiments were performed with a

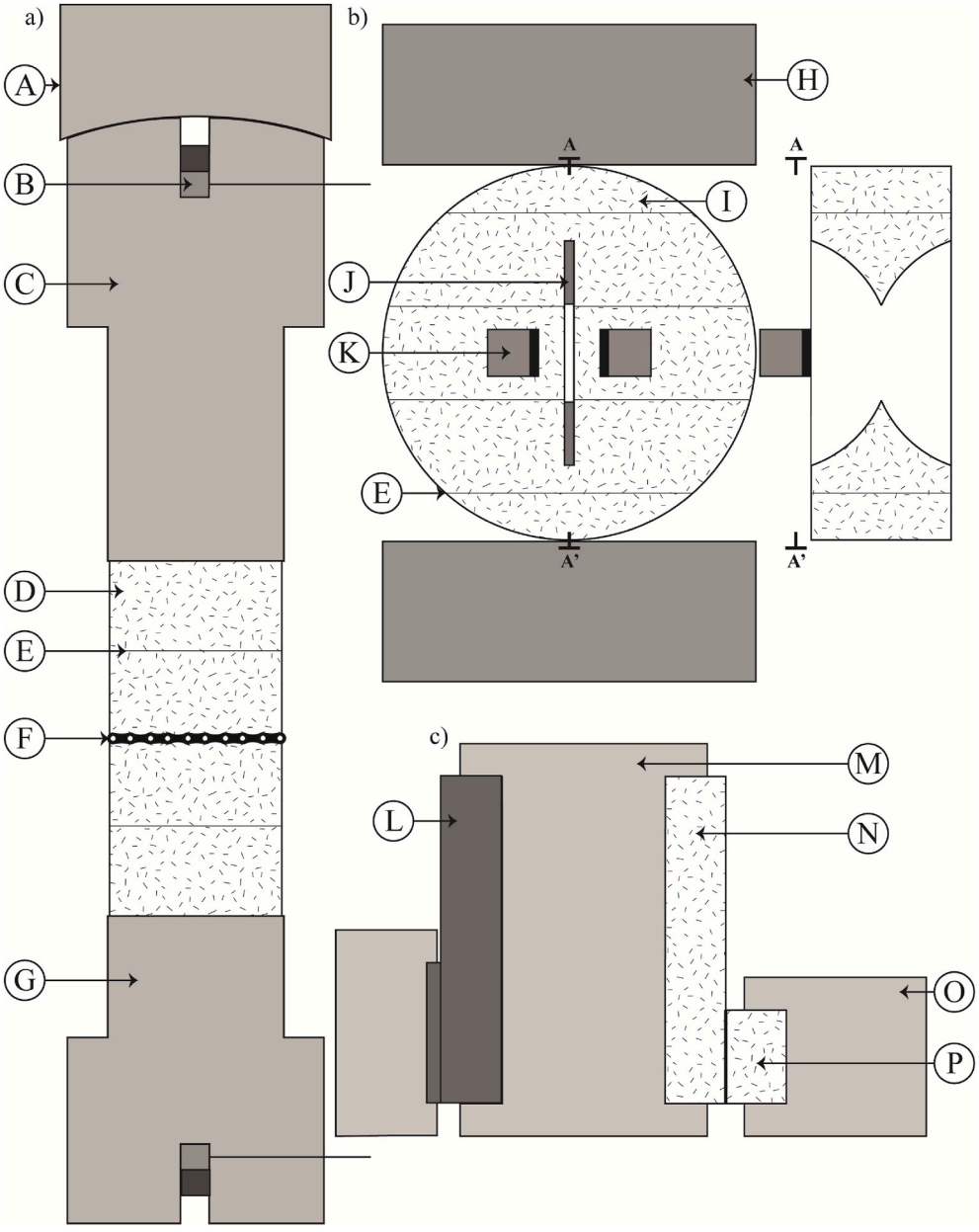

Fig. 2. Experimental setup used for a) uniaxial compression experiments, b) fracture toughness experiments and c) friction experiments. A) ball joint to prevent misalignments, B) piezoelectric sensors, C) top piston, D) uniaxial compression sample, E) bedding plane (perpendicular to the direction of compression), F) chain to attach an extensometer to measure radial deformations, G) bottom piston, H) large piston used for fracture toughness experiments, I) CCNBD sample, J) machined crack of the CCNBD sample, K) "L-shape" metal plates glued on the sample to attach an extensometer and measure the crack mouth opening, L) frictionless assembly, M) large sample holder, N) large sample for friction experiments, O) small sample holder, P) small sample for friction experiments. Note that for saturated experiments, the saturated samples were immersed into distilled water during the experiments.

hydraulic press from Walter and Bai company. Samples were inserted between two pistons placed under the press (Fig. 2a). The top piston is equipped with a ball joint to prevent any misalignment (Fig. 2aA). The equipment allows for an axial stress up to 1 GPa (±50-kPa resolution) on 36 mm diameter samples. During the sample deformation, axial displacements were measured using two linear optoelectronic transducers mounted close to the sample, with a precision of 1 μm. Radial displacements were measured with an extensometer mounted on a chain at the centre of the sample with a 1-μm precision (Fig. 2aF). In addition, wideband (200–950 kHz) piezoelectric sensors were placed in each piston (Fig. 2aB) to monitor the high-frequency Acoustic Emission (AE) events which radiated from the samples during their deformations. The emitted signal was amplified to 40 dB through preamplifiers, and the trigger was set to only record events with an amplitude higher than 0.056 V, that is, ≈1.75 times higher than the background noise of the experimental setup (measured at 0.032 V), preventing noise recording. Each event that fulfilled this condition was recorded at a 1-MHz sampling rate, in a 400 μs window.

After placing the sample between the two pistons, the axial stress was increased by applying a constant displacement rate of 7.2×10^{-4} mm s^{-1} or 5.6×10^{-4} mm s^{-1} for the 72 or 56 mm long samples, respectively, which corresponds to a strain rate of $\dot{\varepsilon}_{ax} \approx 10^{-5}$ s^{-1}. The experiments were stopped after the sample's macroscopic failure. Note that this method follows the ISRM suggested methodology.[47] During sample deformation, the recording rate was set to 0.5 Hz. Each uniaxial compression experiment was performed twice to verify the experimental reproducibility.

The axial displacements were corrected for the elastic distortion of the apparatus (i.e., press column and pistons), calibrated using a metal plug of known stiffness. The axial strain was then inferred from the ratio between the corrected axial displacement and the initial sample length. The radial strain was computed as the ratio between the extension of the chain placed around the sample and its initial perimeter. The volumetric strain was computed by summing the axial strain and twice the radial strain ($\varepsilon_{vol} = \varepsilon_{ax} + 2\varepsilon_{rad}$).

2.2.2. Fracture toughness

The Cracked Chevron-notched Brazilian Disk (CCNBD) geometry was used for fracture toughness measurements. This geometry was chosen because it allows for a stable crack propagation using a relatively simple machined specimen and standard rock testing apparatus. Cores were first diamond drilled to a diameter of 80 mm. Disks were then sawed and opposite faces ground flat (±100 μm) for a final height of 30 mm. Then, a notch was made by inserting 16 mm of a diamond saw (50.95-mm diameter) on both sides of the sample at its centre following the ISRM norms.[48] If bedding planes were observed, the sample was cored parallel and the notched perpendicular to the planes. Fracture toughness was therefore measured perpendicular to the bedding planes (i.e., arrester orientation, Fig. 2b).

For the fracture toughness experiments, the CCNBD samples were placed under the hydraulic press described above (Fig. 2b). Large pistons were attached to the press to facilitate sample positioning (Fig. 2bH). The system allows for an axial force up to 2 MN with a resolution of 0.5 kN. During the sample deformation, axial displacements were measured with two linear optoelectronic transducers mounted close to the sample with a precision of 1 μm. The crack mouth opening (i.e., the horizontal opening of the machined notch) was monitored with an extensometer (±1-μm precision) placed between two "L-shape" metal plates glued on the sample (Fig. 2bK).

After placing the sample under the press with the machined notch aligned parallel to the direction of the applied force, a constant displacement rate of 2.5×10^{-2} mm s^{-1} was applied up to crack propagation. This fast displacement rate was chosen so that the experiments would last less than 10 s, as recommended by the ISRM.[48] During the sample deformation, the recording rate was 0.01 Hz. Note that each fracture toughness experiment was performed twice to verify the experimental reproducibility.

The mode I stress intensity factor at the machined crack tips was computed by[48–52]:

$$K_I = \frac{F_{ax}}{B\sqrt{R}} Y^* \tag{6}$$

where F_{ax} is the axial force applied on the CCNBD sample, B and R are the sample thickness and radius, respectively. For the geometry used,

$$Y^* = u \exp(v\alpha_1) \tag{7}$$

where u and v are constants listed in the ISRM norms and α_1 is the long half machined crack length normalised by the sample radius. The mode I fracture toughness (i.e., critical stress intensity factor), K_{Ic}, of the sample was computed using equations (6) and (7) and for the maximum axial force recorded during the experiment. From the measured K_{Ic} and the computed Young's modulus and Poisson's ratio (inferred from V_p and V_s) the fracture energy, G_c, could by computed assuming plane strain conditions by[53]:

$$G_c = \frac{K_{Ic}^2(1-\nu^2)}{E} = 2\gamma \tag{8}$$

To compute G_c, even if static moduli can be derived from uniaxial compression experiments, to take sample variability into account, we chose to use the dynamic moduli as they can be measured just before the fracture toughness experiment of each sample. Indeed, they are non-destructive measurements, as opposed to uniaxial compression experiments. Note that the values of the static and dynamic moduli are quite similar (Table 3).

2.2.3. Friction

To find the frictional parameters of the tested sample, direct shear experiments were performed in a single shear configuration (also called rock joint testing). Two rectangular cuboids of 70 × 35 × 13 mm and 20 × 35 × 13 mm (±10 μm) were prepared for each experiment (Fig. 2c). The sliding surfaces were polished with a rough abrasive disc (Struers® MDpiano 80, comparable to no. 80 SiC abrasive paper), however, the surface roughness was mostly controlled by the samples grain size and porosity.

The biaxial deformation apparatus was composed of three forcing blocks of stainless steel (Fig. 2c). For simplicity, only one side was used for rock friction (Fig. 2cN and P). On the other side, a frictionless surface (i.e., GLYCODUR®, PTFE-based 3-layers material, with friction <0.02) was used (Fig. 2cL). The apparatus is equipped with a horizontal hydraulic piston providing a normal force to the samples up to 180 kN (±0.04-kN precision), and a vertical piston connected to four high velocity linear motors that apply the shear force up to 193 kN with an accuracy of 0.04 kN. The system allows for the shearing of the sample at velocities ranging from 1 μm s^{-1} to 0.25 m s^{-1}. The horizontal (i.e., normal) and vertical (i.e., shear) displacements are measured with optical encoders having a resolution of 5 nm. For more details on the experimental apparatus, see Violay et al.[54]

After placing the samples in the sample holders (Fig. 2cM and O) and positioning them in the biaxial apparatus, the normal stress was raised slowly at 1 MPa/min up to 5 MPa. Then, the shear stress was increased by applying a constant displacement rate on the vertical piston at 1 μm/s. After 2 mm of displacement, the axial piston was stopped and the shear stress released. The normal stress was raised again to 10 MPa prior to shearing the sample another 2 mm. This procedure was performed 5 times to obtain the frictional behaviour of the sandstones at different normal stress (5, 10, 15, 20 and 25 MPa). During sample deformation, the recording rate was 0.1 Hz. Note that this method follows the ISRM suggested methodology.[55]

The normal and shear displacements were corrected from the elastic distortion of the horizontal and vertical pistons, respectively, calibrated using a metal plug of known stiffness. The normal and shear stresses

applied on the discontinuity (i.e., simulated joint or fault) were computed as the ratio of the normal force and the shear force, respectively, with the sample contact area ($\sigma_n = F_n/A$and $\tau = F_s/A$). The shear stress was corrected for the machine's friction contribution. For each normal stress the static shear stress, τ_s (i.e., the shear stress at the onset of sliding), was picked. The linear regression between the static shear stress and the normal stress applied was computed to obtain the static friction coefficient, μ_s, of the tested rock samples, with a cohesion (C) that is assumed to be 0 (i.e., $\tau_s = \mu_s\sigma_n + C$).

3. Results

3.1. Uniaxial compression

For all the tested sandstones and under both dry and saturated conditions, the mechanical results of the uniaxial compression experiments (Fig. 3 and Fig. 4) follow the classical five stages of deformation. Initially, the axial stress – axial strain curves (Fig 3a and 4b) are non-linear due to the closure of the micro-cracks oriented sub-perpendicular to the direction of compression, as well as to the sample-loading interface's deformation.[56] During this phase, almost no radial strain is observed and no AE events are emitted. Then, the samples show a linear increase in axial stress with the axial and volumetric strain. Again, no AE events are recorded. This phase ends at the onset of dilatancy, a point denoted C' (Fig 3 and 4a and b), which is marked by a deviation from linearity of the axial stress – axial strain and axial stress – volumetric strain curves, as well as an onset of AE events. After C′ is reached, the axial stress versus strain curves follows a non-linear increase until the peak axial stress is reached (Fig 3 and 4a and b), and AE events follow an exponential increase. Ultimately, the sample enters a strain softening phase (i.e., stress drop) and the sample macroscopically fails.

The sample's UCS (peak axial stress) and C′ decay with increasing the sample porosity (Fig. 5). The five tested sandstones present lower C′ and UCS under water-saturated conditions as opposed to dry conditions, i.e., water weakening (Figs. 4 and 5 and Table 3). Under water-saturated conditions, the axial stress at C′ is 97, 92, 83, 96 and 70% of that observed in the dry experiments and the UCS is 90, 92, 77, 95 and 70% of that observed in the dry experiments for FS, BS, AS, RS and DS, respectively. Moreover, water-saturated samples reach C′ and their UCS at lower axial strain values than dry samples (Fig. 4b). AEs are also strongly reduced under water-saturated conditions (Fig. 4c).

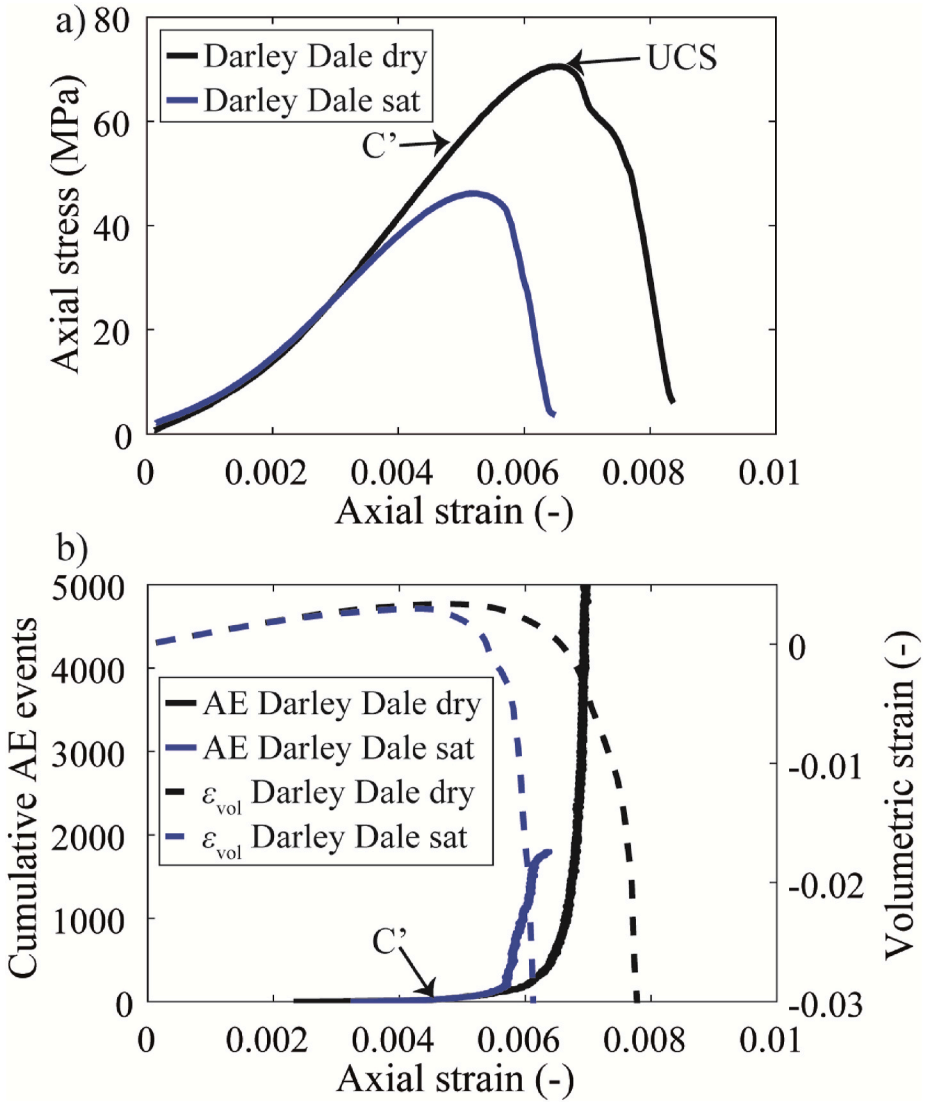

Fig. 3. Mechanical and AE data obtained for the uniaxial compression tests of Darley Dale sandstones deformed under dry and saturated conditions. a) Axial stress as a function of the axial strain, b) cumulative AE events and volumetric strain as a function of the axial strain. An example of C′ and the UCS is shown for a dry sample.

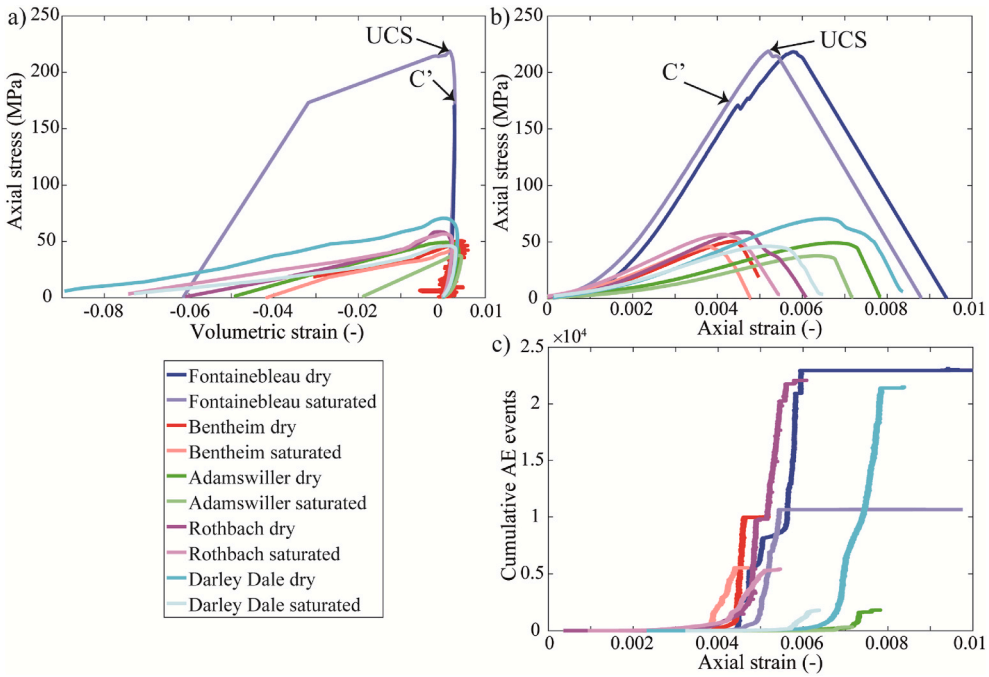

Fig. 4. Mechanical and AE data obtained for the uniaxial compression tests of the five sandstones deformed under dry and water-saturated conditions. a) Axial stress as a function of the volumetric strain, b) axial stress as a function of the axial strain and c) cumulative AE events as a function of the axial strain. An example of C′ and the UCS is shown for a Fontainebleau sandstone experiment performed under water-saturated conditions. Note that the AE data are very well correlated with the mechanical data, presenting an increase in events before and at each stress drop.

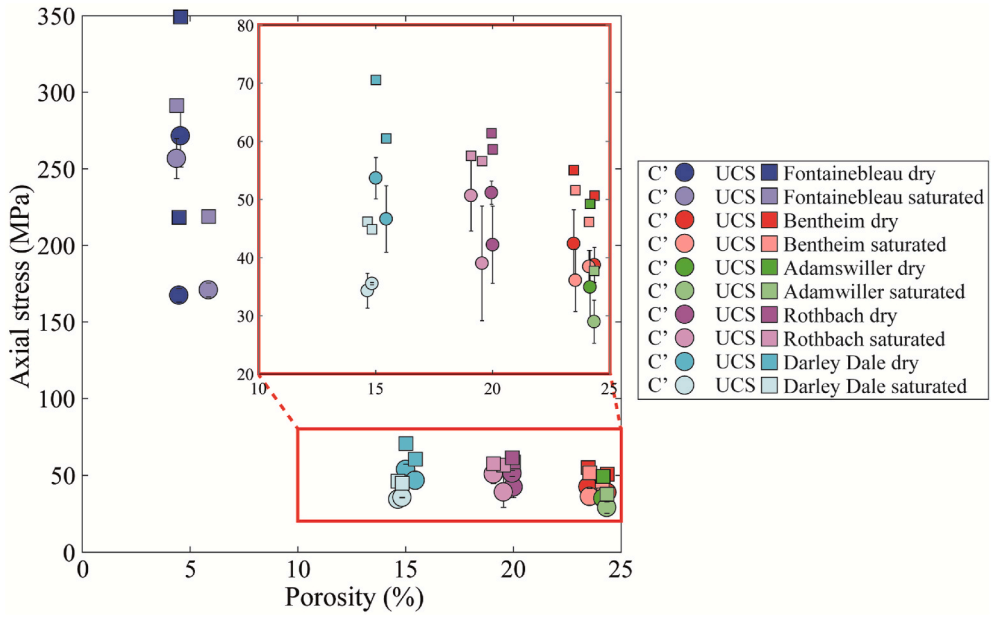

Fig. 5. Axial stress at C′ and the uniaxial compressive strength (UCS) of the five tested sandstones under dry and water-saturated conditions as a function of the initial measured porosity. The red rectangle presents a zoom on BS, AS, RS and DS. For C′ data, the error bars correspond to the difference between the deviation of linearity of the axial stress – axial strain curves and the onset of AE events. (For interpretation of the references to colour in this figure legend, the reader is referred to the Web version of this article.)

3.2. Fracture toughness

For the tested sandstones and both under dry and water-saturated conditions, the mechanical data of the fracture toughness experiments all show similar trends (Fig. 6). First, the data show a quasi-linear increase of K_I as a function of both the axial displacement and the crack mouth opening, followed by a deviation from linearity prior to reaching a peak (K_{Ic}). After the peak value, a drop in K_I and a large crack mouth opening occur as the sample fractures. Note that all the experiments are considered valid as the sample failed with the formation of a crack aligned with the machined notch (i.e., mode I fracturing), as recommended by the ISRM. A visual inspection of the fractured surface at the end of the experiments revealed that the fractures mainly propagate at the grain junctions and not within the grains.

K_{Ic} is a decreasing function of the porosity (Fig. 7a). Additionally, water-saturated samples failed at a lower value of K_{Ic} than dry samples (Fig. 7a and Table 3). Indeed, K_{Ic} under water-saturated condition is 10, 6, 25, 18 and 34% lower than under dry conditions for FS, BS, AS, RS and DS, respectively (Fig. 7a). Similar results are found for the fracture energy, G_c, with a reduction of 44, 21, 49, 43 and 52% for FS, BS, AS, RS and DS, respectively (Fig. 7b).

3.3. Friction

For all the tested sandstones and under both dry and water-saturated conditions, the friction data show similar behaviour (Fig. 8). At all the normal stresses, first, a linear increase of the shear stress as a function of the horizontal displacement is observed (Fig. 8a). During this phase, the

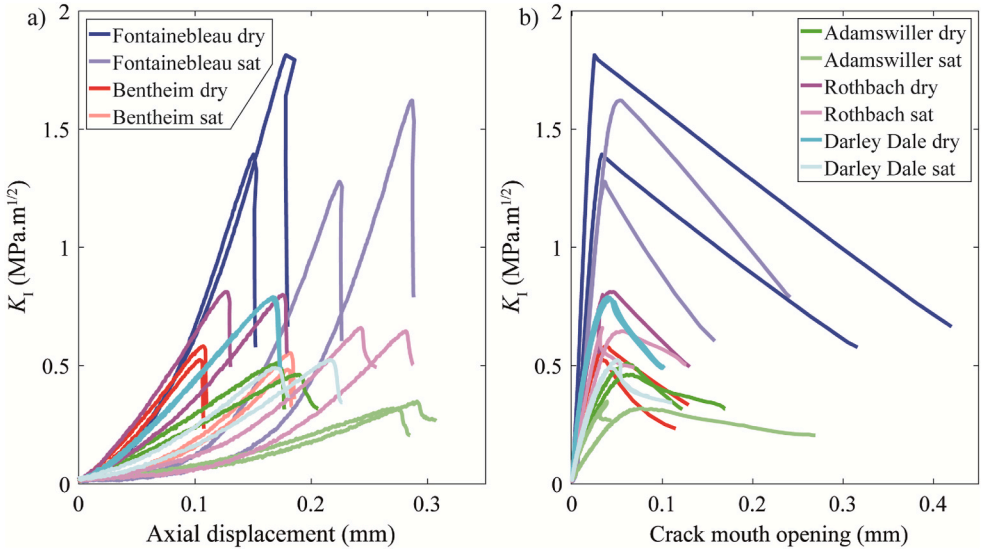

Fig. 6. Mechanical data of the fracture toughness experiments: mode I stress intensity factor as a function of a) the axial displacement and b) the crack mouth opening for the five tested sandstones under dry and water-saturated conditions (sat). The peak value of the recorded K_I is the critical stress intensity factor (or fracture toughness), K_{Ic}, of the sample. For the experiments performed on Bentheim sandstone under water-saturated conditions, the crack mouth opening data were not recorded due to the detachment of the "L-shape" metal plates holding the extensometer at the beginning of the experiments. Importantly, the post-peak behaviour is not to be considered as the crack length has increased (i.e., α_1 increases in equation (7), modifying the computation of K_I).

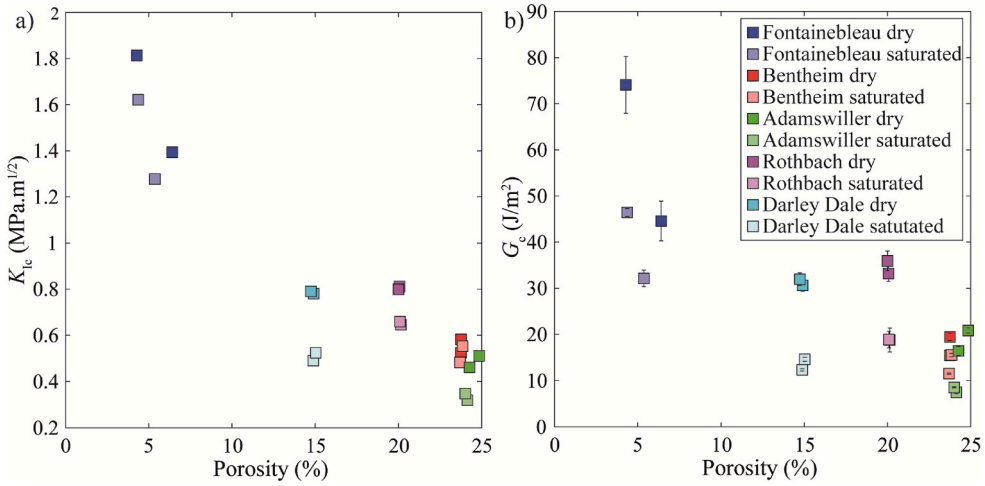

Fig. 7. a) Fracture toughness and b) fracture energy as a function of the sample's initial porosity for the five tested sandstones under both dry and water-saturated conditions.

discontinuity (i.e., simulated joint or fault) is stuck (i.e., not moving) and the sample deforms elastically. This phase ends when the shear stress reaches the shear strength, and the joint starts to slide (red circle in Fig. 8a). The shear stress at the onset of sliding as a function of the normal stress form a single line, with the slope being the friction coefficient (μ_s), and the y-intercept being the joint cohesion (C) (Fig. 8b–f). After the onset of sliding, the sample continues to slide at an almost constant shear stress, and typically reaches a steady-state value equal to, or slightly lower than, μ_s (Fig. 8a). Note that for FS, and at elevated normal stresses (i.e., $\sigma_n \geq 15$ MPa), unstable slip behaviour was observed, as indicated by stick-slip sequences. Also note that, for BS, AS, RS and DS, the samples collapsed at elevated normal stresses.

The experiments demonstrate that the static friction coefficients of the water-saturated samples are generally lower than that of the dry samples (Fig. 8 and Table 3). Indeed, the static friction coefficients are 18, 16 and 19% lower for FS, AS and DS under water-saturated conditions compared to dry conditions. They are, however, equivalent under both conditions for BS and RS. Note that no trend of the static friction coefficient with the porosity could be found.

4. Discussion

The experimental results show that, among the five tested sandstones, water-saturated conditions (compared to dry conditions) cause a reduction in: i) the fracture toughness and fracture energy; and ii) the static friction coefficient, which can explain the reduction of the UCS, as well as the onset of dilatancy.

In the following, the effect of water weakening on sandstone strength and the possible involved mechanisms are discussed. Micro-mechanical models are described and used to interpret and discuss the mechanisms involved in the water weakening.

4.1. Water weakening of sandstone

The performed uniaxial compression experiments showed that the UCS is reduced by 10, 8, 23, 5 and 30% for FS, BS, AS, RS and DS, respectively, in presence of water compared to dry conditions. Note that for FS, due to the sample strength variability under similar condition, no clear conclusion can be drawn on the water weakening. Similar water weakening values of strength can be found in the literature. For DS, Baud et al.[1] measured a triaxial strength water weakening ranging from 12 to 17%. Other studied sandstones present similar weakening values

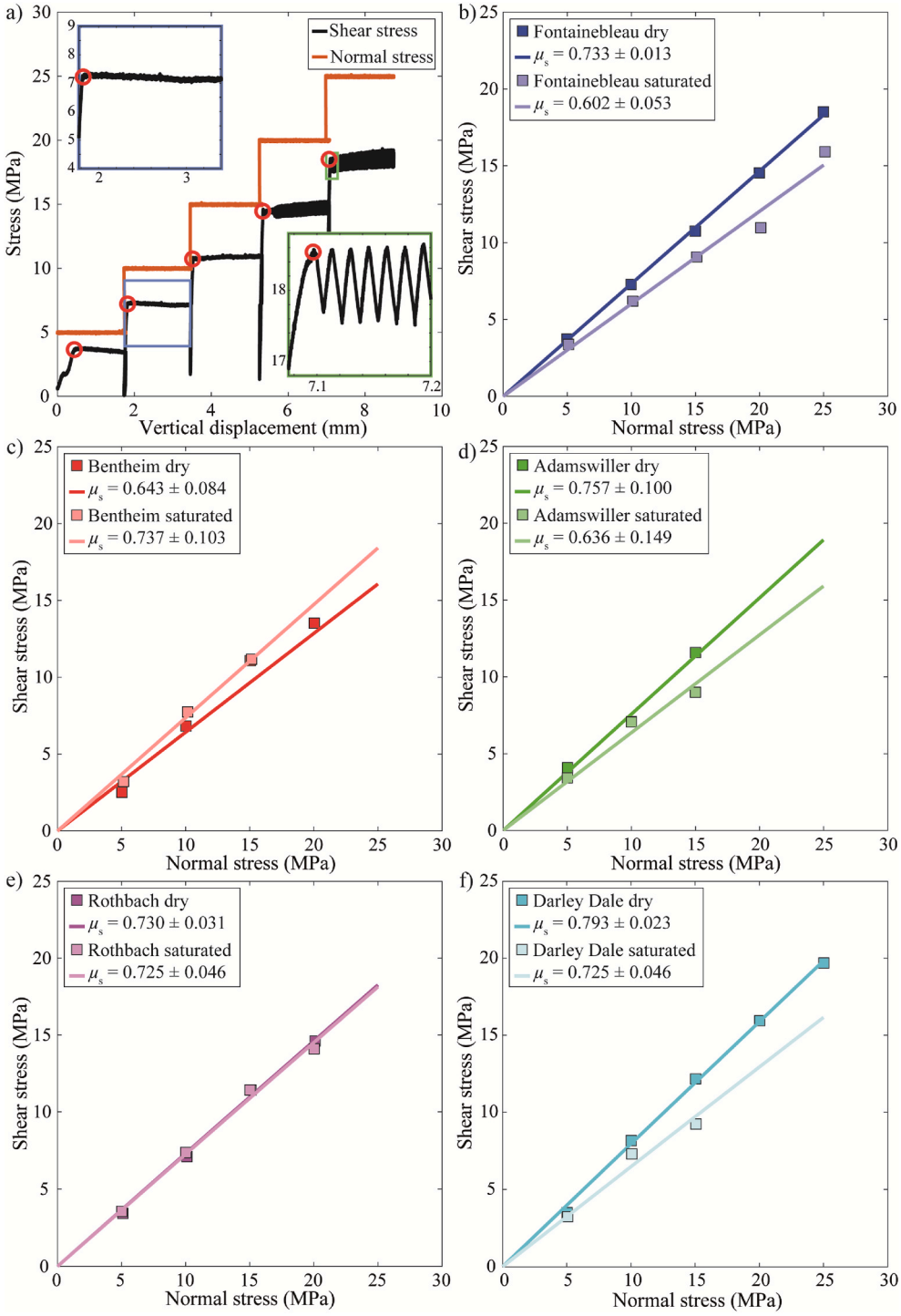

Fig. 8. Friction experiment data obtained for the five tested sandstones under dry and water-saturated conditions. a) shear and normal stresses as a function of the vertical displacement (i.e. shear direction) for a typical friction experiment (FS under dry conditions). For all the normal stresses, red circles show the shear stress at the onset of sliding used to compute the static friction coefficient and cohesion. Additionally, two zooms are presented to show two typical behaviours observed: The blue box presents a zoom on an example of stable sliding where the sample static friction and steady-state friction are equivalent. The green box presents a zoom on unstable sliding behaviour where the cumulative slip is accommodated through stick-slips. Picked shear stress at the onset of sliding as a function of the applied normal stress for b) FS, c) BS, d) AS, e) RS and f) DS under dry and water-saturated experiments. The best fit of the data following $\tau = \mu_s \sigma_n$ is presented for the five tested sandstones under both dry and water-saturated conditions. The value of μ_s is presented in the figures' legends. Note that for BS, AS, RS and DS the sample collapsed at elevated normal stresses. (For interpretation of the references to colour in this figure legend, the reader is referred to the Web version of this article.)

that typically range from 8 to 50%.[1,3,12,19,21] Finally, for FS, previous measurements have also shown no significant strength reduction with the presence of water.[2,22]

Under compressive loading, the macroscopic brittle failure of a rock occurs by damage/micro-crack nucleation, propagation and coalescence.[23–25] In turn, the physical parameters that define the aptitude of cracks to nucleate and propagate are the fracture toughness (or fracture energy) and the static friction coefficient. Interestingly, our experimental results demonstrate that both the mode I fracture toughness and the static friction coefficient of the tested sandstones are reduced in the presence of water (Fig 7 and 8), in agreement with Baud et al.[1] Indeed, among the five tested sandstones, water saturation (compares to dry conditions) causes a reduction of: the fracture toughness and fracture energy ranging from 6 to 35% and 21–52%, respectively, and the static friction coefficient ranging from 0 to 19%. This is in agreement with previous results on sandstones and other rocks, where water saturation was previously found to reduce K_{Ic} [32–35,57] and μ_s, [26–29] see Table 4–6. However, the rock strength weakening, as well as K_{Ic} and μ_s, are variable depending on the tested rock sample, raising the question: What is controlling the efficiency of the water weakening in rocks?

The experiments performed show that the porosity has no influence on sandstone weakening (Fig. 5). This is in agreement with the study of Hawkins & McConnell[3] performed on sandstones with initial porosities ranging from about 2 to 40%. Hawkins & McConnell,[3] however, found a

Table 3
Summary of the static Young's modulus (E_s), the UCS, K_{Ic} and μ_s obtained experimentally under both dry and water-saturated conditions.

Sample	Dry static Young's modulus,	Saturated static Young's modulus,	Dry uniaxial compressive strength,	Saturated uniaxial compressive strength,	Water weakening of the strength,	Dry fracture toughness,	Saturated fracture toughness,	Water weakening of the fracture toughness,	Dry static friction coefficient,	Saturated static friction coefficient,	Water weakening of the static friction coefficient,
	E_s^{dry} (GPa)	E_s^{sat} (GPa)	UCS^{dry} (MPa)	UCS^{sat} (MPa)	UCS^{sat}/UCS^{dry}	K_{Ic}^{dry} (MPa.m$^{1/2}$)	K_{Ic}^{sat} (MPa.m$^{1/2}$)	$K_{Ic}^{sat}/K_{Ic}^{dry}$	μ_s^{dry}	μ_s^{sat}	μ_s^{sat}/μ_s^{dry}
Fontainebleau	59.8	58.7	283.75 ± 92.6	255.05 ± 52.3	0.90	1.60 ± 0.30	1.45 ± 0.24	0.91	0.733	0.720	0.82
Bentheim	15.3	15.4	52.86 ± 3.1	48.87 ± 3.9	0.92	0.55 ± 0.04	0.52 ± 0.05	0.95	0.643	0.737	1.15
Adamswiller	10.4	8.9	49.23	37.73	0.77	0.49 ± 0.03	0.33 ± 0.02	0.67	0.757	0.636	0.84
Rothbach	17.1	17.3	60.01 ± 2.0	57.06 ± 0.7	0.95	0.81 ± 0.01	0.65 ± 0.01	0.80	0.730	0.725	0.99
Darley Dale	15.1	15.2	65.55 ± 7.1	45.53 ± 0.9	0.70	0.79 ± 0.01	0.51 ± 0.02	0.65	0.793	0.646	0.81

correlation between the mineral content and the efficiency of the water weakening of the sandstones: The sensitivity to water increases with higher clay mineral content, and decreases for high quartz content. To investigate the effect of quartz and clay-minerals, and more generally of mineral composition, on the water weakening effect, we computed the normalised onset of dilatancy C' and the normalised UCS, that is, the ratio between the axial stress of the water-saturated experiments and of the dry ones ($\sigma_{ax}^{sat}/\sigma_{ax}^{dry}$). These were plotted as a function of the principal mineral content of the sandstones obtained from X-ray crystallography analysis (Fig. 9). This comparison revealed a mixed effect of the mineral composition. Indeed, no clear trend can be seen on the water weakening of UCS and the mineral content (Fig. 9).

Table 4
Literature data for uniaxial and triaxial strength under both dry and water-saturated conditions.

Sample	Effective confining pressure, P_c-P_f (MPa)	Dry strength (MPa)	Saturated strength (MPa)	Saturated strength/Dry strength	reference
Darley Dale	10	126	110	0.87	Baud et al. (2000)[1]
	30	190	163	0.86	
	50	263	217	0.83	
Berea	10	115	36	0.31	
	40	186	83	0.45	
Pegnant	0	253	144	0.57	Hadizadeh and Law (1991)[19]
Flechtingen	0	82	55	0.67	Zang et al. (1996)[21]
Ruhr	20	211	215	1.02	Duda and Renner (2013)[2]
Wilkeson	20	181	160	0.88	
Fontainebleau	20	616	586	0.95	
Bentheim	30	184	183	0.99	Reviron et al. (2009)[22]
Fontainebleau	0	71	77	1.08	
Applecross	0	141.3	99.3	0.7	Hawkin and McConnell (1992)[3]
Donegal Quartzite	0	237.9	184	0.77	
Basal Quartzite	0	247	202.1	0.82	
Brownstones	0	152	107.4	0.71	
Pilton	0	173.3	152.2	0.88	
Upper Cromhall	0	161.4	143.9	0.89	
Millstone Grit	0	59.3	39.6	0.67	
Holcombe Brook Grit	0	119.1	49	0.41	
Siliceous Sandstone	0	198.4	182.2	0.92	
Elland Flags	0	59.9	31.4	0.52	
Thornhill Rock	0	89.9	38.4	0.43	
Middle Coal Measures	0	37.1	25.3	0.68	
Crackington Formation	0	298.2	232.3	0.78	
Pennant	0	114.2	50	0.44	
Annan	0	66.3	43.6	0.66	
Penrith	0	66	53.1	0.8	
Redcliffe	0	36.1	22.4	0.62	
Midford Sands	0	23.2	14.6	0.63	
Ardingly	0	42.2	36.9	0.87	
Ashdown	0	30.6	32.3	1.06	
Greensand	0	10.5	2.3	0.22	
Voltzia unit	0	152.4	105.1	0.69	Heap et al. (2019)[20]
Intermédiaires unit	0	147	99.5	0.68	
Karlstal unit	0	101.4	76.9	0.76	
Rehberg unit	0	102.1	56.5	0.55	
Trifels unit	0	90.9	60	0.66	
Annweiler unit	0	244	188.8	0.77	
Anté-Annweiler unit	0	82.1	45.8	0.56	
Adamswiller	0	42.5	32.7	0.77	
Rothbach	0	57.8	43.6	0.75	
Fontainebleau	0	283.75 ± 92.6	255.05 ± 52.3	0.90	This study
Bentheim	0	52.86 ± 3.1	48.87 ± 3.9	0.92	
Adamswiller	0	49.23	37.73	0.77	
Rothbach	0	60.01 ± 2.0	57.06 ± 0.7	0.95	
Darley Dale	0	65.55 ± 7.1	45.53 ± 0.9	0.70	

Table 5
Literature data of fracture toughness under both dry and water-saturated conditions. RH = Relative Humidity.

Sample	Dry fracture toughness, K_{Ic}^{dry} (MPa.m$^{1/2}$)	Saturated fracture toughness, K_{Ic}^{sat} (MPa.m$^{1/2}$)	Fracture toughness water weakening, $K_{Ic}^{sat}/K_{Ic}^{dry}$	reference	comment
Dholpur sandstone	0.37	0.25	0.68	Guha Roy et al. (2017)[35]	
Jabalpur white sandstone	0.79	0.54	0.68		
Jabalpur red sandstone	1.05	0.74	0.7		
Jharia shale	0.31	0.15	0.48		
Kumamoto andesite	1.91 ± 0.03	1.66 ± 0.05	0.87	Nara et al. (2012)[33]	here dry is for 20 < RH<30% and saturated for 80 < RH<90%
Oshima granite	2.14 ± 0.09	2.06 ± 0.06	0.96		
Berea sandstone	0.36 ± 0.01	0.30 ± 0.01	0.83		
Shirahama sandstone	0.73 ± 0.01	0.39 ± 0.02	0.53		
Kushiro sandstone	0.89 ± 0.07	0.60 ± 0.02	0.67		
Monroe County sandstone	0.44 ± 0.08	0.22 ± 0.04	0.5	Maruvanchery and Kim (2019)[32]	
Kunming sandstone	0.51 ± 0.01	0.29 ± 0.01	0.57	Zhou et al. (2018)[57]	here, saturated corresponds to a water content of 3.5%
Fontainebleau sandstone	1.60 ± 0.30	1.45 ± 0.24	0.91	This study	
Bentheim sandstone	0.55 ± 0.04	0.52 ± 0.05	0.95		
Adamswiller sandstone	0.49 ± 0.03	0.33 ± 0.02	0.67		
Rothbach sandstone	0.81 ± 0.01	0.65 ± 0.01	0.80		
Darley Dale sandstone	0.79 ± 0.01	0.51 ± 0.02	0.65		

Table 6
Literature data of the frictional parameter under both dry and water-saturated conditions.

Sample	Dry static friction coefficient, μ_s^{dry}	Saturated static friction coefficient, μ_s^{sat}	Water weakening of the static friction coefficient, μ_s^{sat}/μ_s^{dry}	reference	comment
Hawkesbuy sansdtone	0.52	0.47	0.90	Jaeger (1959)[29]	
Granitic gneiss	0.71	0.61	0.86		
Westerly granite	0.60	0.60	1	Byerlee (1967)[26]	
Westerly granite	0.85 to 1.00	0.55 to 0.65	0.65	Dieterich and Conrad (1984)[27]	
Xujiahe Formation sandstone	0.73	0.70	0.96	Zhang et al. (2019)[30]	Experiments at temperature ranging from 30 to 120 °C
Fontainebleau sandstone	0.733	0.602	0.82	This study	
Bentheim sandstone	0.643	0.737	1.15		
Adamswiller sandstone	0.757	0.636	0.84		
Rothbach sandstone	0.730	0.725	0.99		
Darley Dale sandstone	0.793	0.646	0.81		

To further investigate the effect of mineral content on the sandstone deformations, the normalised mode I fracture toughness (i.e., ratio between water-saturated K_{Ic}^{sat} and the average dry K_{Ic}^{dry}) and the normalised static friction coefficient (i.e., ratio between the water-saturated and the dry static friction coefficients, μ_s^{sat}/μ_s^{dry}) were also computed, and plotted against the principal mineral content (Fig. 10 and Fig. 11). The results do not suggest a clear effect of the mineral content on the water weakening of K_{Ic}: A non-clear trend may be drawn suggesting that water weakening efficiency is increased with decreasing the quartz content (Fig. 10a) and increasing phyllosilicate content (Fig. 10b). None of the other mineral contents show any trend. Finally, no influence of the mineral content can be seen on the water weakening effect of μ_s (Fig. 11). These results are in agreement with previous studies (see Table 4–6), where no direct correlations between lithology or mineralogy and water weakening of K_{Ic} and μ_s, were found. Then, what are the mechanisms involved in K_{Ic} and μ_s reduction in presence of water?

The reduction of μ_s under water saturated conditions may originate from either a decrease of the adhesion forces at the contact point, and/or an asperity strength reduction.[27] However, the present data do not allow for the distinction of one or the other mechanism to prevail. For the reduction of K_{Ic} under water saturated conditions, it has been interpreted by previous study to originate from: stress corrosion,[31] mineral dissolution,[32] capillary forces at the crack tip,[33] clay weakening,[34] grain contact lubrication,[35] or a reduction of surface energy via adsorption mechanisms.[1] In the experiments performed, the reduction of the surface energy in presence of water is the most plausible. Indeed, the surface energy of quartz (main mineral in the tested sandstones composition) drop from an estimated value of about 2000 mJ m^{-2} in vacuum, to 406–458 mJ m^{-2} at 100% room humidity, and to 335–385 mJ m^{-2} under water saturated conditions.[58] Such reductions are in agreement with the obtained reduction of K_{Ic} under water-saturated conditions compared to dry conditions (see equation (8)).

Additionally, for UCS, the strain at failure was found to be much lower for water-saturated experiments compared to dry. Similar behaviour was measured for Buntsandstein sandstone deformation under uniaxial compression.[20] However, such behaviour is inhibited, or even reversed, as soon as confining pressure, as low as 2.5 MPa, is applied during the deformation of the samples.[1,20] One possible cause of lower strain at failure under water saturated and uniaxial compression conditions compare to dry, is that water presence helps at localizing the deformation. This process would be inhibited as soon as a confining pressure is applied, as confining pressure also favour localized

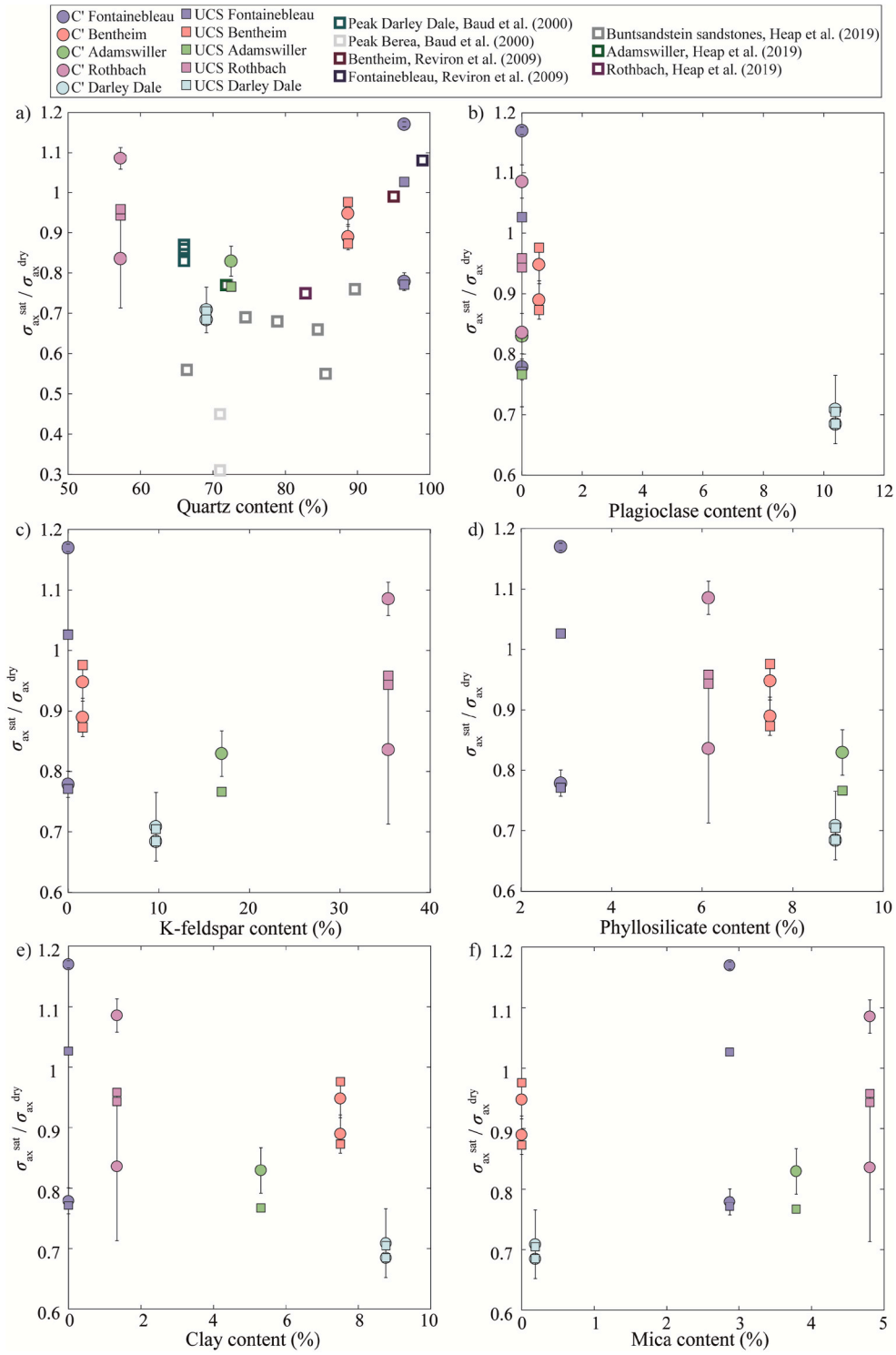

Fig. 9. Normalised axial stress at the onset of dilatancy C′ and normalised peak stress as a function of the rock mineral content: a) quartz, b) plagioclase, c) K-feldspar, d) phyllosilicate, e) clay and f) mica. For C′ data, the error bars correspond to the picking difference between the deviation of linearity of the axial stress – axial strain curves and the onset of AE events. For quartz content, literature data are also reported.[1,20,22]

deformations (see Paterson & Wong,[59] section 3.2 and reference therein). Note however, that the macroscopic post-mortem inspection of the tested sandstone did not reveal significant deformation localisation comparing dry and water saturated experiments (see supplementary materials).

4.2. Micro-mechanical interpretation of water weakening under uniaxial compression

In this section, first, two micro-mechanical models are described: a pore emanating cracks model and a wing crack model. These models are then used to predict the water weakening of sandstones. Time-dependent effects (such as subcritical crack growth) are not considered in these models. Our experiments were performed at high loading

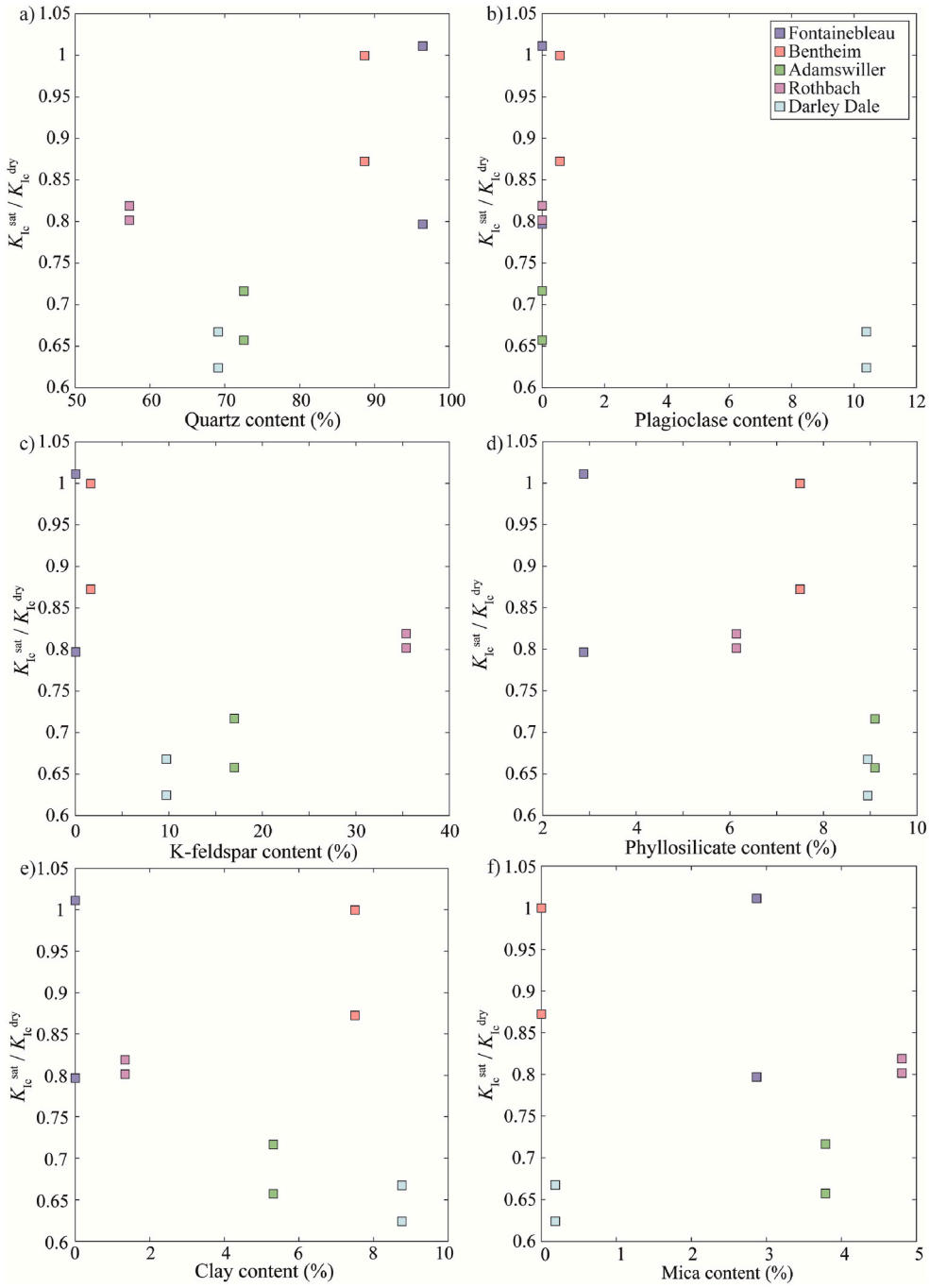

Fig. 10. Normalised fracture toughness (i.e., ratio between water-saturated K_{Ic} and the average dry K_{Ic}) as a function of the rock mineral content: a) quartz, b) plagioclase, c) K-feldspar, d) phyllosilicate, e) clay and f) mica.

rates, limiting such mechanisms.

The pore emanating cracks and a wing crack models were chosen because they are widely used in the geo-mechanical community and because they represent the two extreme cases of crack nucleation and damage growth initiated from geometrical defects,[23] which we believe are relevant for sandstones.

4.2.1. Description of micro-mechanical models

The pore emanating cracks model was developed by Sammis & Ashby.[60] It considers an isotropic elastic medium of initial porosity ϕ made of spherical pores of radius a_{pore}, subjected to axial stress (σ_{ax}). While the axial stress is increased, stress concentrations occur at the poles of the pores with tensile stress oriented perpendicular to σ_{ax}. A pair of cracks of length l emanating from each pore is subjected to mode I stress intensity factor K_I. Cracks grow when the stress intensity factor reaches a critical value (i.e., the fracture toughness) K_{Ic}. With the crack length increasing, the cracks start to interact, facilitating their propagation. Under uniaxial compression, the crack's length as a function of the remote stress applied is given by[60]:

$$\sigma_{ax}(l) = \frac{K_{Ic}}{\sqrt{\pi a_{pore}}} \frac{1}{\left(\frac{1.1\sqrt{\frac{l}{a_{pore}}}}{\left(1+\frac{l}{a_{pore}}\right)} + \frac{\sqrt{2}}{\pi}\sqrt{\phi}\sqrt{\frac{l}{a_{pore}}+1} \right)} \quad (9)$$

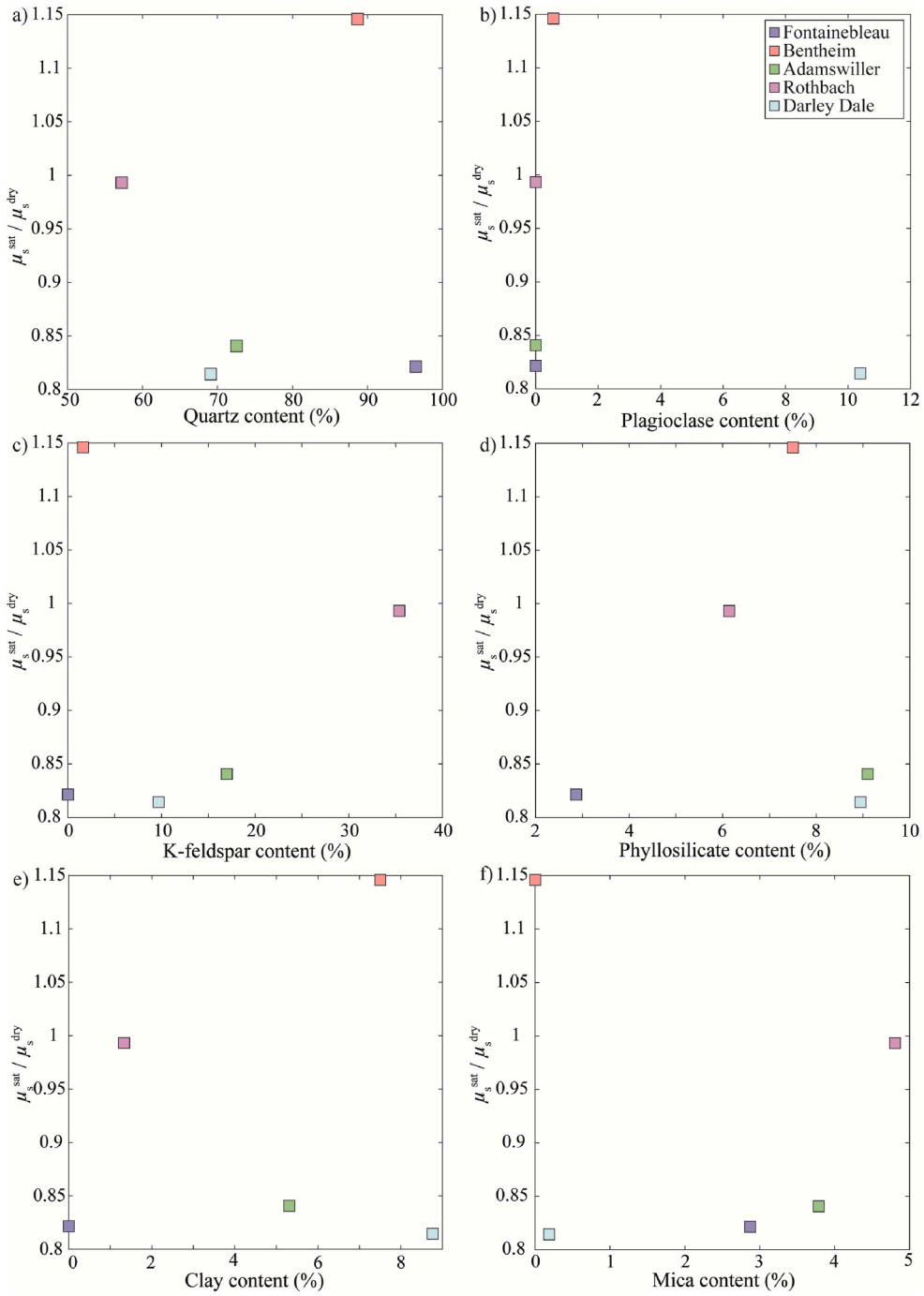

Fig. 11. Normalised static friction coefficients (i.e., ratio between water-saturated and dry μ_s) as a function of the rock mineral content: a) quartz, b) plagioclase, c) K-feldspar, d) phyllosilicate, e) clay and f) mica.

Equation (9) has a maximum value of σ_{ax} corresponding to the UCS of the rock sample. Note that the analytical simplification can be found in Baud et al.[61] Considering that dry and water-saturated rock samples have the same initial porosity (ϕ) and pore radius (a_{pore}), the pore emanating cracks model predicts that the ratio of the UCS for saturated and dry rock samples is simply the ratio of the fracture toughnesses under saturated and dry conditions:

$$\frac{UCS^{sat}}{UCS^{dry}} = \frac{K_{Ic}^{sat}}{K_{Ic}^{dry}} \tag{10}$$

where the subscripts sat and dry stand for the water-saturated and dry parameters, respectively.

The wing crack model was developed by Ashby & Sammis.[23] It considers an isotropic elastic medium containing uniformly-spaced penny-shaped cracks of half-length a_{crack} oriented at an angle θ from σ_{ax}. When the axial stress is increased, a shear stress τ and a normal stress σ_n are transmitted to the inclined cracks. When the shear stress overcomes the frictional strength of the cracks' surfaces (i.e. when $\tau > \mu_s\sigma_n$), the cracks start to slide. This sliding generates tensile stresses at the tips of the inclined cracks. If the resolved stress intensity, K_I, at the inclined crack tips overcomes the fracture toughness K_{Ic} of the material, wing cracks nucleate. Under uniaxial conditions, the initiation of the wing cracks occurs on the most favourably oriented cracks at[62,63]:

$$\sigma_{C'} = \frac{\sqrt{3}}{\sqrt{1+\mu_s^2}-\mu_s}\frac{K_{Ic}}{\sqrt{\pi a_{crack}}} \tag{11}$$

Further increase of the axial stress causes the wing cracks to grow, resulting in their eventual interaction. Under uniaxial conditions, the remote uniaxial stress and the wing crack length are linked by[23]:

$$\sigma_{ax}(l) = \frac{K_{Ic}}{\sqrt{\pi a_{crack}} A_1 (c_1 + c_2)} \tag{12}$$

$$\text{with } A_1 = \pi\sqrt{\frac{\beta}{3}}\left(\sqrt{1+\mu_s^2} - \mu_s\right)$$

$$c_1 = \pi^{-2}\left(\frac{l}{a_{crack}} + \beta\right)^{-\frac{3}{2}} \tag{13}$$

$$c_2 = \frac{2(\pi\alpha)^{-2}\sqrt{\frac{l}{a_{crack}}}}{D_0^{-\frac{2}{3}} - \left(1+\frac{l}{\alpha a_{crack}}\right)^2} \tag{14}$$

where $\alpha = \cos(\theta)$ is the projection of the inclined crack on the plane parallel to the axial stress, $D_0 = \frac{4}{3}\pi N_V(\alpha a)^3$is the initial damage of the sample, $N_V = \rho_{crack}/a_{crack}^3$ is the number of cracks per unit volume (with ρ_{crack} being the initial crack density), and β is an empirical parameter to restrict K_I to finite values when l is small. Equation (11) has a maximum value of σ_{ax}, corresponding to the UCS of the rock sample. Note that an analytical simplification can be found in Baud et al.[61] Considering that dry and water-saturated rock samples have the same initial crack radius (a_{crack}) and crack density (ρ_{crack}), the wing crack model predicts that the ratio between saturated and dry stresses at C′ and the UCS are equivalent:

$$\frac{UCS^{sat}}{UCS^{dry}} = \frac{K_{Ic}^{sat}/A_1^{sat}}{K_{Ic}^{dry}/A_1^{dry}} = \frac{K_{Ic}^{sat}\Big/\left(\sqrt{1+\left(\mu_s^{sat}\right)^2}-\mu_s^{sat}\right)}{K_{Ic}^{dry}\Big/\left(\sqrt{1+\left(\mu_s^{dry}\right)^2}-\mu_s^{dry}\right)} = \frac{\sigma_{C'}^{sat}}{\sigma_{C'}^{dry}} \tag{15}$$

To summarize, taking the ratio between the UCSs performed under water-saturated and dry conditions (i.e., UCS^{sat}/UCS^{dry}) as a proxy for water weakening effect, one can notice that while the pore emanating cracks model predicts only a fracture toughness dependency, the wing crack model predicts both that the fracture toughness and the static friction coefficient influence the water weakening of the rock strength.

4.2.2. Water weakening: experimental data and models prediction

Inserting the measured fracture toughness (K_{Ic}) and static friction coefficient (μ_s) under dry and water-saturated conditions, we now compare the predictions of the effect of water on sandstone's UCS and axial stress at C′ from the pore emanating cracks model and the wing crack model (i.e., equations (10) and (15), respectively), and the UCS and C′ obtained through experimental testing (Fig. 12).

As predicted by the wing crack model (equation (15)), the experimental water weakening of the axial stress at C' and the UCS are of similar magnitude for the majority of the tested sandstones. Additionally, both models predict a water weakening effect on the UCS of the tested sandstones. The models are in good agreement with some experimental data. In particular, the pore emanating cracks model accurately predicts the water weakening at the UCS for DS, and both models accurately predict the weakening of FS and BS. However, in the majority of cases, both models overestimate (by about 10–20%) the water weakening of the tested sandstones.

The systematic overestimations of the water weakening effect might arise from three possible causes:

1) The use of macroscopically (centimeter scale) measured K_{Ic} and μ_s while the micro-mechanical models require micro-scale mechanical parameters. In sandstones, factures can propagate at both the grain junction and within the minerals. In the performed fracture toughness experiments, characterization of the post-mortem samples revealed that fractures mostly propagate at grain junctions, with K_{Ic} values of 1.60, 0.55, 0.49, 0.81 and 0.79 MPa $m^{1/2}$ under dry conditions and 1.45, 0.52, 0.33, 0.65 and 0.51 MPa $m^{1/2}$ under water-saturated conditions for FS, BS, AS, RS and DS, respectively. These values are lower than those of the sandstones' constituted materials. Indeed, quartz, orthoclase (i.e., K-feldspar) and albite (i.e., Na-plagioclase), have K_{Ic} values of 1.5 ± 0.3, 1.1 ± 0.4 and 0.78 ± 0.06 MPa $m^{1/2}$, respectively.[64,65] Therefore, if during uniaxial compression of sandstones, cracks do not only propagate at the grain junction but also within the grains, higher values than the those obtained with CCNBD samples must be used. Additionally, μ_s was also not measured at the micro-scale. Indeed, in the preformed friction experiments we tested the resistance to motion of surfaces composed of many grains. In the wing crack model, the friction that needs to be overcome to induce a stress intensity factor at the crack tip is the friction of the inclined cracks. In the case of sandstones, the inclined cracks are grain contacts with very variable roughnesses due to the grain shapes and/or interlocking, which can lead to a higher value of the micro-scale static friction coefficient compared to the macro-scale one. Importantly, water's effect at microscale can differ from the one at macroscale. Further, the use of macroscopically measured K_{Ic} and μ_s, while the micro-mechanical models require micro-scale mechanical parameters, should strongly affect the absolute values of K_{Ic} and μ_s, albeit the ratio between dry and water-saturated measurements are probably affected much less.

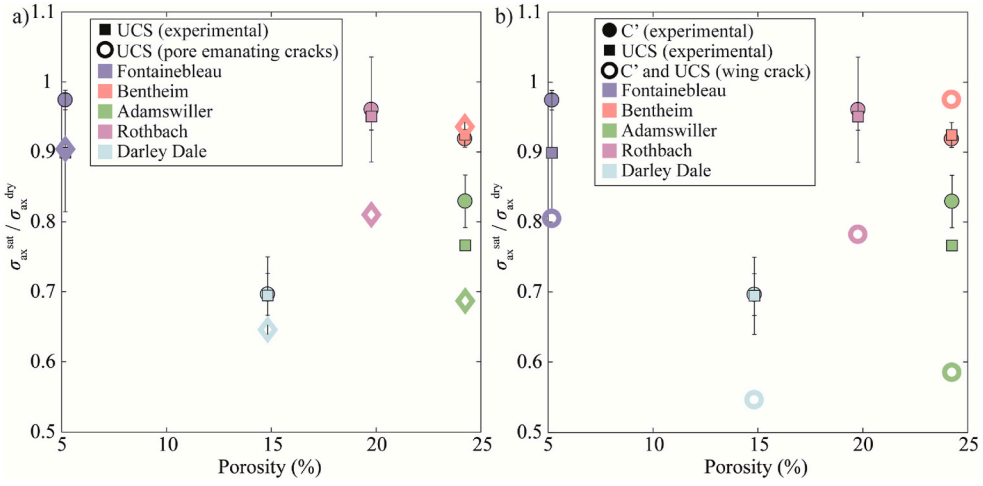

Fig. 12. The ratios of axial stress at C' (circles) and the uniaxial compressive strength (squares and diamonds) between water-saturated and dry experiments obtained experimentally (full symbols) and obtained via a) the pore emanating cracks model, and b) the wing crack model as a function of the sample porosity. The colour corresponds to the rock tested. Note that water-weakening dependence in the pore emanating cracks model is present only in K_{Ic} (equation (10)), while for the wing crack model it is present in both K_{Ic} and μ_s (equation (15)). (For interpretation of the references to colour in this figure legend, the reader is referred to the Web version of this article.)

2) The micro-mechanical models are, as all models, oversimplifying the mechanisms at hand. Even if our tests were performed under room-pressure conditions, water-saturated experiments can be affected by drainage conditions during fast crack propagation. However, considering the high porosity/permeability of the tested sandstones, undrained conditions are quite unlikely.

4.2.3. *Extrapolation to water weakening under triaxial conditions*

Under triaxial conditions, no expressions of the pore emanating cracks model exist in the literature for conventional loading. Therefore, only the wing-crack model is discussed here. This model is highly used in the geo-mechanics community and in general allows for a satisfactory explanation of experimental data (see Ashby & Sammis,[23] section 4) and water weakening (see above section). The important variables to determine rock strength are: 1) the static friction coefficient of the cracks (μ_s), 2) the initial flow size (i.e., the initial half inclined crack length a_{crack}), 3) the mode I fracture toughness of the material (K_{Ic}), and 4) the initial damage (D_0). Usually, those parameters are found through a best fit of the experimental data. Trying to infer these parameters is not trivial. Even if several authors have shown that K_{Ic} is a pressure dependent parameter, with higher values at higher confining pressures,[66–75] the experiments performed here resulted in consistent values of K_{Ic} and μ_s (see paragraph 4.2.2 for a discussion on the use of obtained parameters into micro-mechanical models). However, trying to infer a_{crack} and D_0 physically is challenging, particularly for sedimentary rocks, when crack length and number of cracks are hardly assessable. In order to understand how these four parameters influence the prediction of sandstone strength, a parametric study was performed. We compared the strength of Darley Dale sandstone, under dry and water-saturated conditions, predicted by the wing crack model under triaxial conditions (see Ashby & Sammis,[23] for a description of the model under triaxial stress) and obtained experimentally (UCS from this study and triaxial strength from Bud et al.[1]) (Fig. 13). DS was chosen as it presents the highest water weakening of the tested samples. In each panel of Fig. 13, one parameter is taken as a variable while reference values are used for the 3 others, i.e., K_{Ic} = 0.785 MPa m$^{1/2}$ (measured for dry Darley Dale), μ_s = 0.8036 (measured for dry Darley Dale), a_{crack} = 110 μm (= half of the average grain size measured via an optical microscopic survey), and D_0 = 0.44 (from Baud et al. (2000) for dry Darley Dale sandstone). This parametric study demonstrates that the four parameters have a huge impact on the modeled strength. For example, for the reference parameters taken, changing D_0 from 0.1 to 0.7, a_{crack} from 100 to 1000 μm, K_{Ic} from 0.1 to 1.9 MPa m$^{1/2}$, or μ_s from 0.2 to 1, multiplies the modeled UCS by 2.5, 3.1, 19, and 2, respectively. Additionally, it shows that D_0 and μ_s are controlling the dependency on the effective confining pressure ($P_c - P_f$), i.e., the slope of the predicted strength as a function of the effective confining pressure (Fig. 13a and d); and a_{crack} and K_{Ic} are controlling the y-intercept, i.e., changing a_{crack} or K_{Ic} moves the curve to a parallel prediction in the strength – effective confining pressure diagram (Fig. 13b and c). Allowing the four parameters free to fit the data leads to many possible outcomes which explain the experimental data. Note however, that for dry conditions, using K_{Ic} and μ_s measured in this study coupled with D_0 estimated by Baud et al.[1] (i.e., 0.44), provides an excellent strength prediction for samples where 500 < a_{crack} < 800 μm (values close to the linear extent of the grain junction observed under an optical microscope (Fig. 1)). For water-saturated

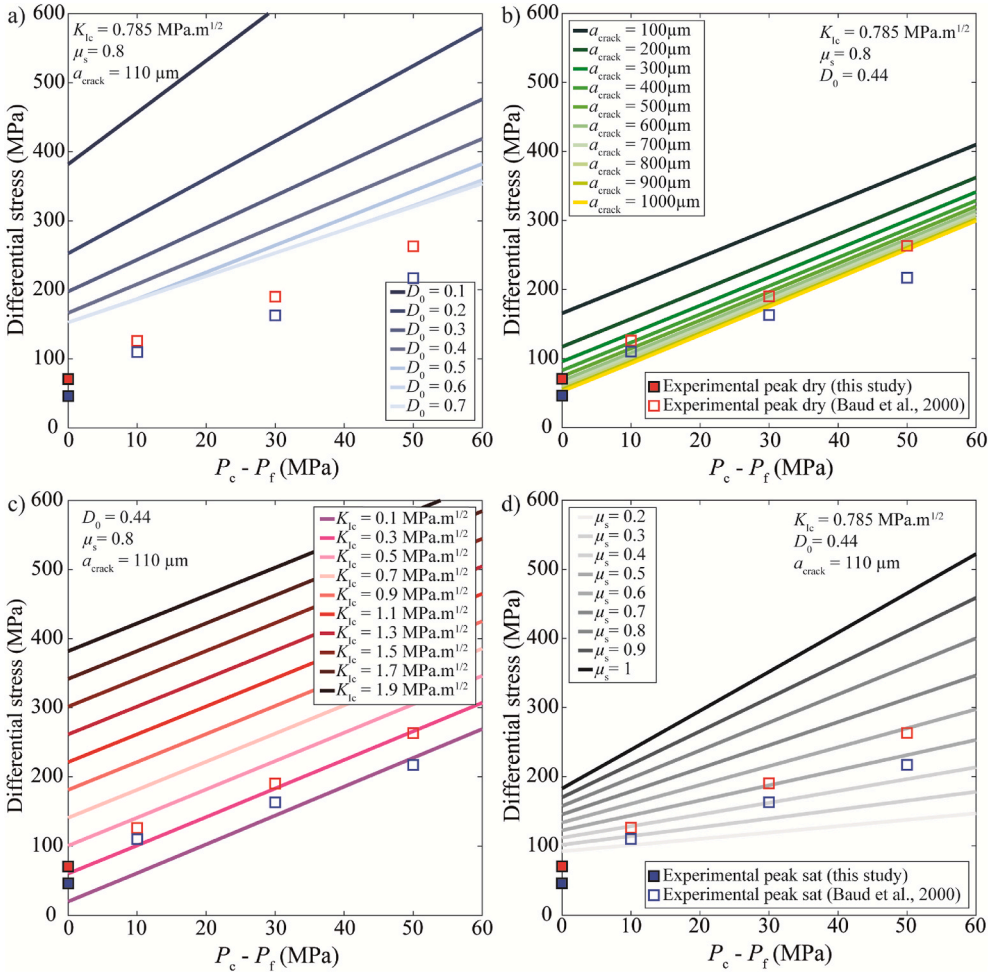

Fig. 13. Parametric study of the influence of a) the initial damage, b) the initial flow size, c) the mode I fracture toughness, and d) the static friction coefficient on triaxial strength predicted by the wing crack model for dry and water-saturated (sat) Darley Dale sandstone. For reference, the UCS measured here and triaxial strength measured by Baud et al.[1] are plotted. The reference parameters used (when they are fixed) are: K_{Ic} = 0.785 MPa m$^{1/2}$ (measured for dry Darley Dale), μ_s = 0.8 (measured for dry Darley Dale), a_{crack} = 110 μm (= half of the average grain size measured via an optical microscopic survey), and D_0 = 0.44 (from Baud et al.[1] for dry Darley Dale sandstone). For all, θ (crack angle compared to the direction of compression) is taken to be 30°.

conditions, using K_{Ic} and μ_s measured in this study, the model provides a satisfactory strength prediction for a_{crack} = 500 μm and D_0 = 0.25. Additionally, C' and the strength predicted by the wing crack model hold for other sandstones.[1,61]

5. Conclusions

More than 50 destructive (uniaxial compression, fracture toughness and friction) experiments, complemented by more than 100 non-destructive (porosity and ultra-sonic) measurements have been used to better understand the effect of the presence of fluid on the short-term strength of five sandstones. The samples' UCSs and fracture toughnesses are directly linked to the measured initial porosities. Additionally, water saturation (compare to a dry sample) causes a reduction of i) the fracture toughness and fracture energy by 6–35% and 21–52%, respectively; ii) the static friction coefficient by 0–19%, explaining the reduction of the UCS and onset of dilatancy by 0–30%. The mechanisms of the water weakening on the sandstones' compressive strengths are directly linked to the reduction of the fracture toughnesses (or equivalently of the fracture energies) and to the static friction coefficients of the materials. However, the mechanisms involved in the water weakening of the fracture toughnesses and static friction coefficients are complex and future experimental investigations are needed to better constrain the processes at hand.

The introduction of the experimentally-measured fracture toughnesses and static friction coefficients into micro-mechanical models (the pore emanating cracks model and wing crack model) has been used to predict the water weakening of the sandstones' uniaxial compressive strengths. It has been shown that the models predict the water weakening relatively well, with a general slight overestimation (10–20%). Finally, a parametric analysis was performed on the wing crack model, revealing that a sandstone's absolute strength can be estimated by means of physical and mechanical parameter measurements.

Declaration of competing interest

The authors declare that they have no known competing financial interests or personal relationships that could have appeared to influence the work reported in this paper.

Acknowledgment

This work was funded by Gaznat SA (Grant FRICTION: Fault Reactivation during CO2 sequestraTION). Marie Violay thanks the ERC project BEFINE (Grant 757290). This work of the Interdisciplinary Thematic Institute GeoT, as part of the ITI 2021–2028 program of the University of Strasbourg, CNRS and Inserm, was supported by IdEx Unistra (ANR-10-IDEX- 0002), and by SFRI-STRAT'US project (ANR ANR-20-SFRI-001) under the framework of the French Investments for the Future Program. The authors thanks Nicolas Brantut for providing Darley Dale sandstone. The authors thanks Thierry Adatte for XRD performing the analysis. The authors also thank Barnaby Fryer for proofreading. Raw data can be found at https://zenodo.org/.

Appendix A. Supplementary data

Supplementary data to this article can be found online at https://doi.org/10.1016/j.ijrmms.2021.104916.

References

1 Baud P, Zhu W, Wong T. Failure mode and weakening effect of water on sandstone. *J Geophisical Res Solid Earth*. 2000;105(B7):16371–16389. https://doi.org/10.1029/2000JB900087.
2 Duda M, Renner J. The weakening effect of water on the brittle failure strength of sandstone. *Geophys J Int*. 2013;192(3):1091–1108. https://doi.org/10.1093/gji/ggs090.
3 Hawkins AB, McConnell BJ. Sensitivity of sandstone strength and deformability to changes in moisture content Sandstones studied. *Q J Eng Geol Hydrogeol*. 1992;25:115–130. https://doi.org/10.1144/GSL.QJEG.1992.025.02.05.
4 Lisabeth HP, Zhu W. Effect of temperature and pore fluid on the strength of porous limestone. *J Geophys Res Solid Earth*. 2015;120(9):6191–6208. https://doi.org/10.1002/2015JB012152.
5 Nicolas A, Fortin J, Regnet JB, Dimanov A, Gúeguen Y. Brittle and semi-brittle behaviours of a carbonate rock: influence of water and temperature. *Geophys J Int*. 2016;206(1):438–456. https://doi.org/10.1093/gji/ggw154.
6 Zhu W, Baud P, Vinciguerra S, Wong T. Micromechanics of brittle faulting and cataclastic flow in Alban Hills tuff. *J Geophys Res Solid Earth*. 2011;116(B6). https://doi.org/10.1029/2010JB008046.
7 Zhu W, Baud P, Vinciguerra S, Wong T. Micromechanics of brittle faulting and cataclastic flow in Mount Etna basalt. *J Geophys Res Solid Earth*. 2016;121(6):4268–4289. https://doi.org/10.1002/2016JB012826.
8 Terzaghi K, Peck RB, Mesri G. *Soil Mechanics in Engineering Practice*. third ed. John Wiley & Sons; 1996.
9 Handin J, Hager RVJ, Friedman M, Feather JN. Experimental deformation of sedimentary rocks under confining pressure: pore pressure tests. *Am Assoc Pet Geol*. 1963;47(5):717–755.
10 Heard HC. Transition from brittle fracture to ductile flow in Solenhofen limestone as a function of temperature, confining pressure, and interstitial fluid pressure. In: Griggs D, Handin J, eds. *Rock Deformation*. 79. Geological Society of America Memoirs; 1960:193–226.
11 Robinson LHJ. Effect of pore and confining pressures on failure characteristics of sedimentary rocks. *Soc Pet Eng*. 1959;216:26–32.
12 Baud P, Reuschlé T, Ji Y, Cheung CSN, Wong T. Mechanical compaction and strain localization in Bleurswiller sandstone. *J Geophys Res Solid Earth*. 2015;120(9):6501–6522. https://doi.org/10.1002/2015JB012192.
13 Simmons CJ, Freiman SW. Effect of corrosion processes on subcritical crack growth in glass. *J Am Ceram Soc*. 1981;64(11):683–686. https://doi.org/10.1111/j.1151-2916.1981.tb15870.x.
14 Freiman SW. Effect of chemical enviroments on slow crack growth in glasses and ceramics. *J Geophys Res*. 1984;89(B6):4072–4076. https://doi.org/10.1029/JB089iB06p04072.
15 Michalske TA, Freiman SW. Stress corrosion of ceramic materials. *J Am Ceram Soc*. 1983;66(4).
16 Anderson OL, Grew PC. Stress corrosion theory of crack propagation with applications to geophysics. *Rev Geophys*. 1977;15(1):77–104. https://doi.org/10.1029/RG015i001p00077.
17 Atkinson BK. Subcritical crack growth in geological materials. *J Geophys Res*. 1984;89(B6):4077–4114. https://doi.org/10.1029/JB089iB06p04077.
18 Rutter EH. Pressure solution in nature, theory and experiment. *J Geol Soc London*. 1983;140(5):725–740. https://doi.org/10.1144/gsjgs.140.5.0725.
19 Hadizadeh J, Law RD. Water-weakening of sandstone and quartzite deformed at various stress and strain rates. *Int J Rock Mech Min Sci Geomech Abstr*. 1991;28(5):431–439. https://doi.org/10.1016/0148-9062(91)90081-V.
20 Heap MJ, Villeneuve M, Kushnir ARL, Farquharson JI, Baud P, Reuschlé T. Rock mass strength and elastic modulus of the Buntsandstein: an important lithostratigraphic unit for geothermal exploitation in the Upper Rhine Graben. *Geothermics*. 2019;77:236–256. https://doi.org/10.1016/j.geothermics.2018.10.003.
21 Zang A, Wagner CF, Dresen G. Acoustic emission, microstructure, and damage model of dry and wet sandstone stressed to failure. *J Geophys Res Solid Earth*. 1996;101(B8):17507–17521. https://doi.org/10.1029/96JB01189.
22 Reviron N, Reuschlé T, Bernard JD. The brittle deformation regime of water-saturated siliceous sandstones. *Geophys J Int*. 2009;178(3):1766–1778. https://doi.org/10.1111/j.1365-246X.2009.04236.x.
23 Ashby MF, Sammis CG. The damage mechanics of brittle solids in compression. *Pure Appl Geophys*. 1990;133(3):489–521. https://doi.org/10.1007/BF00878002.
24 Brace WF, Paulding BW, Scholz C. Dilatancy in the fracture of crystalline rocks. *J Geophys Res*. 1966;71(16):3939–3953. https://doi.org/10.1029/JZ071i016p03939.
25 Brace WF, Bombolakis EG. A note on brittle crack growth in compression. *J Geophisical Res*. 1963;68(12):3709–3713.
26 Byerlee J. High confining pressure some experiments made. *J Geophys Res*. 1967;72(14):3639–3648. https://doi.org/10.1029/JZ072i014p03639.
27 Dieterich JH, Conrad G. Effect of humidity on time- and velocity-dependent friction in rocks. *J Geophys Res*. 1984;89(B6):4196–4202. https://doi.org/10.1029/jb089ib06p04196.
28 Rutter EH. The influence of interstitial water on the rheological behaviour of calcite rocks. *Tectonophysics*. 1972;14(1):13–33. https://doi.org/10.1016/0040-1951(72)90003-0.
29 Jaeger JC. The frictional properties of joints in rock. *Geofis Pura e Appl*. 1959;43(1):148–158. https://doi.org/10.1007/BF01993552.
30 Zhang Q, Li X, Bai B, Hu H. The shear behavior of sandstone joints under different fluid and temperature conditions. *Eng Geol*. 2019;257(105143). https://doi.org/10.1016/j.enggeo.2019.05.020.
31 Kataoka M, Obara Y, Kuruppu M. Estimation of fracture toughness of anisotropic rocks by semi-circular bend (SCB) tests under water vapor pressure. *Rock Mech Rock Eng*. 2015;48(4):1353–1367. https://doi.org/10.1007/s00603-014-0665-y.
32 Maruvanchery V, Kim E. Effects of water on rock fracture properties: studies of mode I fracture toughness, crack propagation velocity, and consumed energy in calcite-cemented sandstone. *Geomech Eng*. 2019;17(1):57–67. https://doi.org/10.12989/gae.2019.17.1.057.
33 Nara Y, Morimoto K, Hiroyoshi N, Yoneda T, Kaneko K, Benson PM. Influence of relative humidity on fracture toughness of rock: implications for subcritical crack

growth. *Int J Solid Struct*. 2012;49(18):2471–2481. https://doi.org/10.1016/j.ijsolstr.2012.05.009.
34 Wang JJ, Zhu JG, Chiu CF, Zhang H. Experimental study on fracture toughness and tensile strength of a clay. *Eng Geol*. 2007;94(1-2):65–75. https://doi.org/10.1016/j.enggeo.2007.06.005.
35 Guha Roy D, Singh TN, Kodikara J, Das R. Effect of water saturation on the fracture and mechanical properties of sedimentary rocks. *Rock Mech Rock Eng*. 2017;50(10):2585–2600. https://doi.org/10.1007/s00603-017-1253-8.
36 Baud P, Meredith PG. Damage accumulation during triaxial creep of Darley Dale sandstone from pore volumometry and acoustic emission. *Int J Rock Mech Min Sci Geomech Abstr*. 1997;34(3-4). https://doi.org/10.1016/S1365-1609(97)00060-9. Paper No. 024.
37 Baud P, Klein E, Wong T. Compaction localization in porous sandstones: spatial evolution of damage and acoustic emission activity. *J Struct Geol*. 2004;26(4):603–624. https://doi.org/10.1016/j.jsg.2003.09.002.
38 Baud P, Vajdova V, Wong T. Shear-enhanced compaction and strain localization: inelastic deformation and constitutive modeling of four porous sandstones. *J Geophys Res Solid Earth*. 2006;111(B12). https://doi.org/10.1029/2005JB004101.
39 Bésuelle P, Baud P, Wong T. Failure mode and spatial distribution of damage in Rothbach sandstone in the brittle-ductile transition. *Pure Appl Geophys*. 2003;160(5-6):851–868. https://doi.org/10.1007/PL00012569.
40 Bourbié T, Zinszner B. Hydraulic and acoustic properties as a function of porosity in Fontainebleau Sandstone. *J Geophys Res*. 1985;90(B13):11524. https://doi.org/10.1029/JB090iB13p11524.
41 Louis L, Baud P, Wong T. Microstructural inhomogeneity and mechanical anisotropy associated with bedding in rothbach sandstone. *Pure Appl Geophys*. 2009;166(5-7):1063–1087. https://doi.org/10.1007/s00024-009-0486-1.
42 Noël C, Pimienta L, Violay M. Time-dependent deformations of sandstone during pore fluid pressure oscillations: implications for natural and induced seismicity. *J Geophys Res Solid Earth*. 2019;124(1):801–821. https://doi.org/10.1029/2018JB016546.
43 Wong T, David C, Zhu W. The transition from brittle faulting to cataclasic flow in porous sandstones: mechanical deformation. *J Geophys Res*. 1997;102(B2):3009–3025. https://doi.org/10.1029/96JB03282.
44 Guéguen Y, Palciauskas V. *Introduction to the Physics of Rocks*. Princeton, New Jersey: Princeton University Press; 1994.
45 ASTM Standard D2845-08. Standard Test Method for Laboratory Determination of Pulse Velocities and Ultrasonic Elastic Constants of Rock. doi:10.1520/D2845-08.2.
46 Noël C, Passelègue FX, Giorgetti C, Violay M. Fault reactivation during fluid pressure oscillations: transition from stable to unstable slip. *J Geophisical Res Solid Earth*. 2019;124(11):10940–10953. https://doi.org/10.1029/2019JB018517.
47 Suggested ISRM. Methods for determining the uniaxial compressive strength and deformability of rock materials. *Int Soc Rock Mech*. 1979;16(2):137–140.
48 Fowell RJ, Hudson JA, Xu C, Chen JF, Zhao X. Suggested method for determining mode I fracture toughness using Cracked Chevron Notched Brazilian Disc (CCNBD) specimens. *Int J Rock Mech Min Sci Geomech Abstr*. 1995;32(1):57–64. https://doi.org/10.1016/0148-9062(94)00015-U.
49 Fowell RJ, Xu C, Dowd PA. An update on the fracture toughness testing methods related to the cracked Chevron-notched Brazilian disk (CCNBD) specimen. *Pure Appl Geophys*. 2006;163(5-6):1047–1057. https://doi.org/10.1007/s00024-006-0057-7.
50 Fowell RJ, Xu C. The use of the cracked Brazilian disc geometry for rock fracture investigations. *Int J Rock Mech Min Sci Geomech Abstr*. 1994;31(6):571–579. https://doi.org/10.1016/0148-9062(94)90001-9.
51 Fowell RJ, Xu C. The cracked chevron notched Brazilian disc test- geometrical considerations for practical rock fracture toughness measurement. *Int J Rock Mech Min Sci Geomech Abstr*. 1993;30(7):821–824. https://doi.org/10.1016/0148-9062(93)90029-D.
52 Xu C, Fowell RJ. Stress intensity factor evaluation for cracked chevron notched brazilian disc specimens. *Int J Rock Mech Min Sci Geomech Abstr*. 1994;31(2):157–162. https://doi.org/10.1016/0148-9062(94)92806-1.
53 Lawn B. *Fracture of Brittle Solids*. second ed. Cambridge: Cambridge University Press; 1993.
54 Violay M, Giorgetti C, Cornelio C, et al. HighSTEPS: a high strain temperature pressure and speed apparatus to study earthquake mechanics. *Rock Mech Rock Eng*. 2021;54(4):2039–2052. https://doi.org/10.1007/s00603-021-02362-w.
55 Muralha J, Grasselli G, Tatone B, Blümel M, Chryssanthakis P, Yujing J. ISRM suggested method for laboratory determination of the shear strength of rock joints: revised version. *Rock Mech Rock Eng*. 2014;47(1):291–302. https://doi.org/10.1007/s00603-013-0519-z.
56 Korinets A, Alehossein H. On the initial non-linearity of compressive stress-strain curves for intact rock. *Rock Mech Rock Eng*. 2002;35(4):319–328. https://doi.org/10.1007/s00603-002-0030-4.
57 Zhou Z, Cai X, Ma D, Cao W, Chen L, Zhou J. Effects of water content on fracture and mechanical behavior of sandstone with a low clay mineral content. *Eng Fract Mech*. 2018;193:47–65. https://doi.org/10.1016/j.engfracmech.2018.02.028.
58 Parks GA. Surface and interfacial free energies of quartz. *J Geophys Res*. 1984;89(B6):3997–4008. https://doi.org/10.1029/JB089iB06p03997.
59 Paterson M, Wong T. *Experimental Rock Deformation - the Brittle Field*. Springer S.; 2005. https://doi.org/10.1007/b137431.
60 Sammis CG, Ashby MF. The failure of brittle porous solids under compressive stress states. *Acta Metall*. 1986;34(3):511–526. https://doi.org/10.1016/0001-6160(86)90087-8.
61 Baud P, Wong T, Zhu W. Effects of porosity and crack density on the compressive strength of rocks. *Int J Rock Mech Min Sci*. 2014;67:202–211. https://doi.org/10.1016/j.ijrmms.2013.08.031.
62 Ashby MF, Hallam SD. The failure of brittle solids containing small cracks under compressive stress states. *Acta Metall*. 1986;34(3):497–510. https://doi.org/10.1016/0001-6160(86)90086-6.
63 Nemat-Nasser S, Horii H. Compression-induced nonplanar crack extension with application to splitting, exfoliation, and rockburst. *J Geophys Res Solid Earth*. 1982;87(B8):6805–6821. https://doi.org/10.1029/JB087iB08p06805.
64 Whitney DL, Broz M, Cook RF. Hardness, toughness, and modulus of some common metamorphic minerals. *Am Mineral*. 2007;92(2-3):281–288. https://doi.org/10.2138/am.2007.2212.
65 Dal Bó M, Cantavella V, Sánchez E, Hotza D, Gilabert FA. Fracture toughness and temperature dependence of Young's modulus of a sintered albite glass. *J Non-Cryst Solids*. 2013;363(1):70–76. https://doi.org/10.1016/j.jnoncrysol.2012.12.001.
66 Abou-Sayed AS, Brechtel CE, Clifton RJ. In situ stress determination by hydrofracturing: a fracture mechanics approach. *J Geophys Res*. 1978;83(B6):2851–2862. https://doi.org/10.1029/JB083iB06p02851.
67 Al-Shayea NA, Khan K, Abduljauwad SN. Effects of confining pressure and temperature on mixed-mode (I-II) fracture toughness of a limestone rock. *Int J Rock Mech Min Sci*. 2000;37(4):629–643. https://doi.org/10.1016/S1365-1609(00)00003-4.
68 Balme MR, Rocchi V, Jones C, Sammonds PR, Meredith PG, Boon S. Fracture toughness measurements on igneous rocks using a high-pressure, high-temperature rock fracture mechanics cell. *J Volcanol Geoth Res*. 2004;132(2-3):159–172. https://doi.org/10.1016/S0377-0273(03)00343-3.
69 Funatsu T, Seto M, Shimada H, Matsui K, Kuruppu M. Combined effects of increasing temperature and confining pressure on the fracture toughness of clay bearing rocks. *Int J Rock Mech Min Sci*. 2004;41(6):927–938. https://doi.org/10.1016/j.ijrmms.2004.02.008.
70 Gehne S, Forbes Inskip ND, Benson PM, Meredith PG, Koor N. Fluid-driven tensile fracture and fracture toughness in nash point shale at elevated pressure. *J Geophys Res Solid Earth*. 2020;125(2), e2019JB018971. https://doi.org/10.1029/2019JB018971.
71 Kataoka M, Mahdavi E, Funatsu T, et al. Estimation of mode I fracture toughness of rock by semi-circular bend test under confining pressure condition. *Procedia Eng*. 2017;191:886–893. https://doi.org/10.1016/j.proeng.2017.05.258.
72 Schmidt RA, Huddle CW. Effect of confining pressure on fracture toughness of Indiana limestone. *Int J Rock Mech Min Sci*. 1977;14(5-6):289–293. https://doi.org/10.1016/0148-9062(77)90740-9.
73 Stoeckhert F, Brenne S, Molenda M, Alber M. Mode I fracture toughness of rock under confining pressure. In: *Rock Mechanics and Rock Engineering: From the Past to the Future*. 2016:313–318. https://doi.org/10.1201/9781315388502-52. London.
74 Thallak S, Holder J, Gray KE. The pressure dependence of apparent hydrofracture toughness. *Int J Rock Mech Min Sci Geomech Abstr*. 1993;30(7):831–835. https://doi.org/10.1016/0148-9062(93)90031-8.
75 Vásárhelyi B. Influence of pressure on the crack propagation under mode I loading in anisotropic gneiss. *Rock Mech Rock Eng*. 1997;30(1):59–64. https://doi.org/10.1007/BF01020113.